

NASA-CR-199982

ORIGINAL CONTAINS  
COLOR ILLUSTRATIONS  
9

FINAL  
IN-34-CR  
OCIT  
7041  
P62

---

**An Experimental Investigation of  
Flow-Induced Oscillations of the  
Brüel & Kjær In-Flow Microphone**

---

**Richard S. Fields Jr.**

---

A Thesis  
Presented to the Faculty of  
California Polytechnic State University, San Luis Obispo

In Partial Fulfillment of the Requirements for the Degree of  
Master of Science in Aeronautical Engineering

November 1995

(NASA-CR-199982) AN EXPERIMENTAL INVESTIGATION OF FLOW-INDUCED OSCILLATIONS OF THE BRUEL AND KJAER IN-FLOW MICROPHONE M.S. Thesis (California Polytechnic State Univ.) 62 p

N96-19067  
Unclas  
G3/34 0100651

---

**An Experimental Investigation of  
Flow-Induced Oscillations of the  
Brüel & Kjær In-Flow Microphone**

---

**Richard S. Fields Jr.**

---

**A Thesis**

**Presented to the Faculty of**

**California Polytechnic State University, San Luis Obispo**

**In Partial Fulfillment of the Requirements for the Degree of**

**Master of Science in Aeronautical Engineering**

**November 1995**

## Acknowledgments

The author would like to sincerely acknowledge those individuals who made this experiment possible: Paul Soderman who made funding possible and provided invaluable insight to this investigation; Dr. Jin Tso, my thesis advisor, mentor and source of motivation who provided this opportunity and guided me through and through; Chris Allen and Steve Jaeger who provided me with countless bits of advice and information; the NASA Ames machine shop for fabricating the model; Steve Scaglione and Bill Peneff, wind tunnel mechanics/operators; Fred Lemos and Dee Green, my hot-wire support; My parents who made this all possible through support and confidence.

# Table Of Contents

---

<b>SYMBOLS</b>	<b>1</b>
<b>1. INTRODUCTION</b>	<b>2</b>
<b>2 EXPERIMENTAL APPARATUS AND PROCEDURE</b>	<b>5</b>
2.1 ANECHOIC CHAMBER JET FACILITY	5
2.2 MODEL DESIGN AND CONSTRUCTION	6
2.3 MODEL MOUNTING AND ALIGNMENT	8
2.4 SURFACE PRESSURE MEASUREMENTS	9
2.5 CAVITY ACOUSTIC MEASUREMENTS	10
2.6 BOUNDARY LAYER VELOCITY PROFILES	11
<b>3. RESULTS AND DISCUSSION</b>	<b>13</b>
3.1 A COMPARISON OF THE B&K AND FITE MICROPHONES	13
3.1.1 0.25 INCH AND 0.5 INCH B&K MICROPHONES	13
3.1.2 THE 1.5 INCH B&K MICROPHONE MODEL	15
3.1.3 STROUHAL NUMBERS OF MICROPHONE OSCILLATIONS	16
3.2 MEAN FLOW MEASUREMENTS	19
3.2.1 SURFACE PRESSURE MEASUREMENTS	19
3.2.2 MEAN VELOCITY DISTRIBUTIONS	21
3.2.3 VELOCITY DISTURBANCE INTENSITY	26
3.3 SPECTRAL RELATIONSHIP BETWEEN VELOCITY AND ACOUSTIC OSCILLATIONS	30
3.3.1 VELOCITY AND ACOUSTIC SPECTRA	30
3.3.2 COHERENCE BETWEEN VELOCITY AND ACOUSTIC OSCILLATIONS	37
3.4 CAVITY ACOUSTIC OSCILLATION MECHANISMS	41
3.4.1 CAVITY OSCILLATION FREQUENCIES	41
3.4.2 TRAILING-EDGE VORTEX SHEDDING	44
3.4.3 COUPLING WITH CAVITY ACOUSTIC RESONANCE	45
3.4.4 HYDRODYNAMIC PRESSURE OSCILLATIONS	47
3.5 EFFECT OF ADVERSE PRESSURE GRADIENT	47
3.6 EFFECT OF TURBULENCE	48
3.7 EFFECT OF SCREEN	49
<b>4. CONCLUSIONS</b>	<b>54</b>
<b>REFERENCES</b>	<b>56</b>

## List of Figures

Figure 1. Schematic of anechoic chamber free-jet facility at NASA Ames.....	5
Figure 2. Mean velocity profiles measured at successive longitudinal stations.....	6
Figure 3. 0.5 inch and 1.0 inch B&K in-flow microphones and the 1.5 inch model (no screen). .....	7
Figure 4. Microphone model and traverse assembly.....	9
Figure 5. Microphone model configured for surface pressure measurements. ....	10
Figure 6. Microphone model configured for acoustic measurements. ....	11
Figure 7. Instrumentation flow chart.....	12
Figure 8. Acoustic power spectra of 0.25 inch B&K and FITE microphones measured in the NASA Ames 40- by 80- Foot Wind Tunnel: $A_1, B_1$ = dominant tones at $Re_D = 43,951$ ; $a_1, b_1$ = subharmonics of $A_1$ and $B_1$ ; $A'_1, B'_1$ = dominant tones at $Re_D = 52,414$ ; $b'_1$ = subharmonic of $B'_1$ . (Reference 3.).....	14
Figure 9. Acoustic power spectra of 0.5 inch B&K and FITE microphones measured in the NASA Ames 7- by 10- Foot Wind Tunnel: $A_1$ = dominant tone at $Re_D = 52,741$ ; $A'_1$ = dominant tone at $Re_D = 70,330$ ; $A'_2$ and $A'_3$ = second and third harmonics of $A'_1$ . (Reference 3.) .....	15
Figure 10. Acoustic power spectra of the 1.5 inch B&K microphone model: $A_1, A'_1$ , and $A''_1$ = dominant tones at $Re_D = 78,000, 94,000$ , and $110,000$ , respectively; $A_2$ and $A_3$ = second and third harmonics of $A_1$ ; $A'_2$ and $A'_3$ = second and third harmonics of $A'_1$ ; $A''_2$ and $A''_3$ = second and third harmonics of $A''_1$ . .....	16
Figure 11. Strouhal number vs. Mach number for three B&K in-flow microphones. ....	17
Figure 12. Surface pressure distributions obtained by PMARC over (a) the B&K microphone, and (b) the FITE microphone. ....	19
Figure 13. Surface pressure distribution measured over the 1.5 inch B&K microphone model.....	20
Figure 14. Streamwise evolution of mean velocity profiles over the model with no cavity at $Re_D = 110,000$ . .....	22
Figure 15. Streamwise evolution of mean velocity profiles over the model with cavity at $Re_D = 78,000$ . .....	23
Figure 16. Streamwise evolution of mean velocity profiles over the model with cavity at $Re_D = 94,000$ . .....	24
Figure 17. Streamwise evolution of mean velocity profiles over the model with cavity at $Re_D = 110,000$ . .....	25
Figure 18. Streamwise evolution of velocity disturbance intensity over the model with no cavity at $Re_D = 110,000$ . .....	27
Figure 19. Streamwise evolution of velocity disturbance intensity over the model with cavity at $Re_D = 94,000$ .....	28
Figure 20. Streamwise evolution of velocity disturbance intensity over the model with cavity at $Re_D = 110,000$ .....	29
Figure 21. Velocity power spectra over the model with no cavity. $Re_D = 110,000$ . ....	33
Figure 22. Velocity power spectra over the model with cavity. $Re_D = 78,000$ . ....	34
Figure 23. Velocity power spectra over the model with cavity. $Re_D = 94,000$ . ....	35
Figure 24. Velocity power spectra over the model with cavity. $Re_D = 110,000$ . ....	36

Figure 25. Coherence between acoustic and velocity signals over the model with cavity. $Re_D$ = 78,000.....	38
Figure 26. Coherence between acoustic and velocity signals over the model with cavity. $Re_D$ = 94,000.....	39
Figure 27. Coherence between acoustic and velocity signals over the model with cavity. $Re_D$ = 110,000.....	40
Figure 28. Strouhal number comparison of cavity oscillations. The solid line denotes Ethembaoglu's pressure fluctuation spectrum at the downstream cavity wall of a rectangular cavity. (Reference 12.).....	42
Figure 29. Strouhal number vs. cavity aspect ratio. (References 5, 7, 8 and 12.).....	43
Figure 30. Acoustic power spectra of the model with screen removed: $A_1$ = dominant tone at $Re_D$ = 45,000; $A_2$ - $A_7$ = harmonics of $A_1$ .....	49
Figure 31. Velocity power spectra over the model with no screen. $Re_D$ = 45,000.....	51
Figure 32. Coherence between acoustic and velocity signals over the model with no screen. $Re_D$ = 45,000.....	52
Figure 33. Strouhal number comparison of cavity oscillations of the 1.5 inch model with and without the screen. The solid line denotes Ethembaoglu's pressure fluctuation spectrum at the downstream cavity wall of a rectangular cavity. (Reference 12.).....	53

## SYMBOLS

$c$	Speed of sound
$D$	Microphone diameter
$D_j$	Jet diameter
$c_p$	Pressure coefficient
$c_p'$	Fluctuations of pressure coefficient
$f$	Frequency in Hz
$H$	$= \delta^*/\theta$ , boundary layer shape factor
$L$	Cavity length
$M$	Mach number
$R$	Cavity radius
$r$	Transverse coordinate from jet centerline
$R_j$	Jet radius
$Re_D$	$= U_\infty D/\nu$ , Reynolds number based on microphone diameter $D$
$St$	$= fL/U_\infty$ , Strouhal number based on cavity length
$U_\infty$	Free stream velocity
$u'$	Streamwise velocity disturbance intensity
$U_e$	Mean velocity at the boundary layer edge
$W$	Cavity depth
$X$	Streamwise coordinate from model apex
$X_j$	Streamwise coordinate from jet exit
$Y$	Transverse coordinate from model surface
$\delta$	Boundary layer thickness
$\delta_o$	Boundary layer thickness at separation point
$\delta^*$	Boundary layer displacement thickness
$\lambda$	Acoustic wavelength
$\nu$	Kinematic viscosity
$\theta$	Boundary layer momentum thickness

## 1. INTRODUCTION

Aircraft noise has long been an important issue to urban communities surrounding airports. It has received a lot more attention in the past decade when airport noise regulations became increasingly stringent worldwide. Recent interests were also fueled by the sonic boom and the noises during takeoff and landing of the proposed High-Speed Civil Transport (HSCT). This accordingly has increased the demand for reliable aeroacoustic measurements in a controlled environment, like wind tunnels, to evaluate aircraft noise generation sources and mechanisms for various aircraft configurations. It has also increased the demand for lower background noises introduced by wind tunnel test facilities and instruments in order to obtain higher signal-to-noise ratios.

There are numerous sources that contribute to wind tunnel background noises. They include the wind tunnel drive system, flow interaction with the model support, wind tunnel shear layers, and vortex generators, etc.<sup>1,2</sup> In an in-flow measurement, it also includes the microphone self-noise. Typically, an in-flow microphone has a condenser microphone encased in a cavity downstream of an axisymmetric forebody.<sup>3</sup> The cavity has an annular array of orifices that are covered with a fine porous screen to allow the incident sound waves into the cavity. While the forebody shields the encased microphone from direct flow excitations, the microphone is not free from the flow-induced pressure perturbations caused by cavity flow oscillations and wind tunnel turbulence. These flow-induced noises in some cases could be strong enough to mask desired acoustic signals.

For years the Brüel & Kjær (B&K) microphones have been accepted as the industry standard. However, Allen and Soderman<sup>3</sup> as well as Glover and Shivashankara<sup>4</sup> have found that the B&K in-flow microphones generate intense high-frequency tones and high noise floors, which could prevent acquisition of acoustic signals over a broad frequency range. The tones were believed to be flow-induced, although the underlying mechanisms responsible for their growth were not clear. As Allen and Soderman have reported in their study, when the sharp pointed forebody of a B&K microphone is replaced with an elongated blunt-nosed forebody (i.e., the FITE, the Flow Induced Tone Eliminator designed by Allen), such flow-induced tones could be successfully eliminated. Again, the mechanisms for eliminating the self-induced tones were not clear.

The tones could be triggered by boundary-layer instabilities amplified in the adverse pressure region near the microphone cavity. They could be related to strong interactions of cavity shear layer oscillations with the cavity trailing edge. This is supported by the far-field acoustic measurements of a rectangular cavity by Block<sup>5</sup> and her vortical-acoustic feedback model<sup>6</sup>. It is also supported by Sarohia's<sup>7</sup> study of axisymmetric cavities without screens, where distinct cavity shear layer oscillations do occur if the cavity length is greater than a minimum value, and other cavity studies as reviewed extensively by Rockwell and Naudascher<sup>8</sup>.

The tones, of course, could also be the consequence of cavity acoustic resonance.<sup>9,10</sup> In a detailed study of screened cavities, Soderman<sup>10</sup> has suggested that the orifice flow oscillations could be coupled with cavity acoustic pressures to generate tones. In his model,

the cavity acoustic pressures interact with the orifice oscillations in such a way as to amplify those oscillations and lock the frequencies of the oscillations to the cavity modes. In turn the orifice oscillations transfer free-stream energy into the cavity and energize the acoustic modes.

The complex flow inside the cavity and the potential involvement of more than one acoustic oscillation mechanisms explains why it has been difficult to determine the responsible acoustic oscillation mechanism(s) for the B&K in-flow microphone. This is especially so because very little has been done in the past for cavities covered with mesh screens. As a result, an experimental investigation was done to obtain detailed understanding of the flow and acoustic oscillations over the microphone forebody and cavity and to determine the microphone's cavity acoustic oscillation mechanism(s).

## 2 EXPERIMENTAL APPARATUS AND PROCEDURE

The experiment was conducted in the anechoic chamber at the NASA Ames Research Center. A 1.5 inch microphone model, a scaled model of the B&K 0.5 inch UA 0386 in-flow microphone, was constructed and tested in a 7 inch round free jet inside the anechoic chamber in order to examine cavity acoustic oscillations. The key features of the jet facility, the microphone model, and their test instruments and procedures are described in this section.

### 2.1 Anechoic Chamber Jet Facility

The anechoic chamber at NASA Ames consisted of a 7 inch round free jet in a rectangular 25'x18'x11' (wedge tip to wedge tip) room that was anechoic to sound frequencies greater than 150 Hz. As shown schematically in figure 1, the jet flow was supplied by a centrifugal compressor driven by two variable 500 hp General Electric motors. Air from the compressor flowed through a diffuser, an in-flow silencer, a transition duct, and a plenum chamber with a series of screens, before exiting the jet nozzle. The flow was collected on the opposing wall of the jet nozzle by an acoustically treated collector. The flow was collected on the opposing wall of the jet nozzle by an acoustically treated collector.

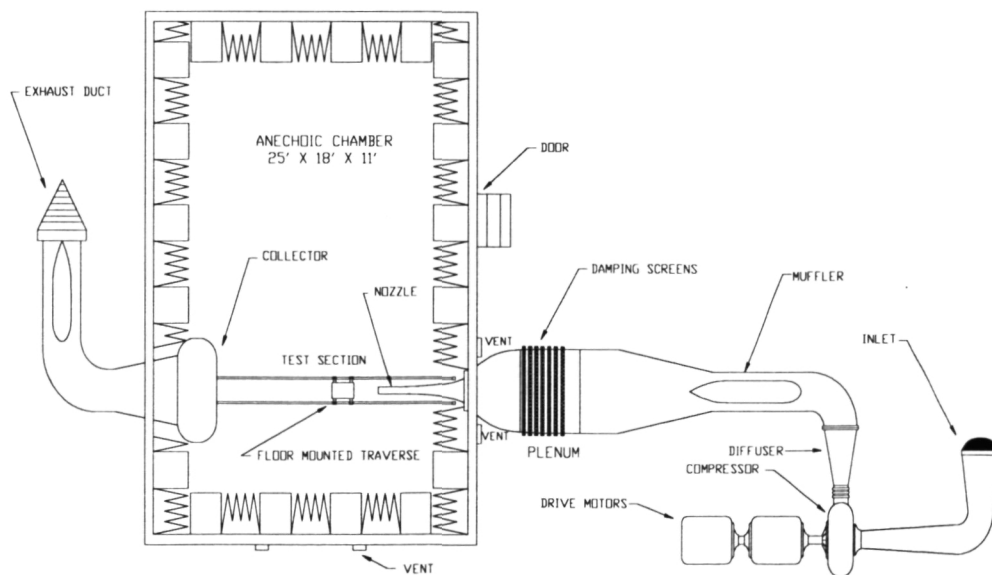


**Figure 1.** Schematic of anechoic chamber free-jet facility at NASA Ames.

The jet Mach number was controlled by changing the motor RPM. As determined by the plenum temperature and pressure, the Mach number could be varied from 0.0 to 0.25. Air flow at the jet exit had the characteristic top-hat velocity profile, as shown in figure 2. This velocity profile was measured with a single hot-wire probe. Same measurements at successive longitudinal stations, also shown in figure 2, showed that the jet potential core was about 5 jet diameters long. Meantime, the turbulence intensity was less than 0.5% on the centerline at  $X_j/D_j=1.5$  for air speeds less than 200 ft/sec.

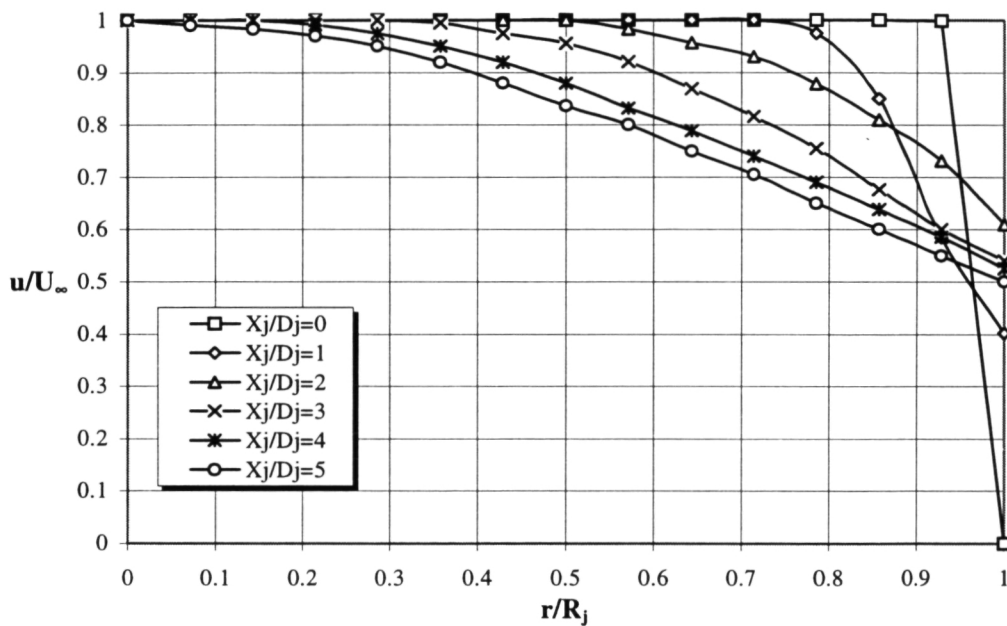


**Figure 2.** Mean velocity profiles measured at successive longitudinal stations.

## 2.2 Model Design and Construction

The 1.5 inch microphone model was designed and constructed to simulate the B&K in-flow microphone cavity oscillations. The model's surface coordinates were obtained from a 0.5 inch B&K UA 0386 microphone, using a computer-controlled feeler and an optical

comparator. The coordinates were then tripled and downloaded into a CNC lathe for machining. The dimensions of the model's cavity on the other hand were obtained by measuring the cavity of a bisected 0.5 inch B&K microphone. The cavity orifices were machined using an electronic discharge technique. Afterwards, a mesh screen, also geometrically scaled, was wound in two layers over the cavity in the same manner as the 0.5 inch B&K microphone. Figure 3 shows the constructed 1.5 inch microphone model in comparison with the 0.5 inch and 1.0 inch B&K microphones.

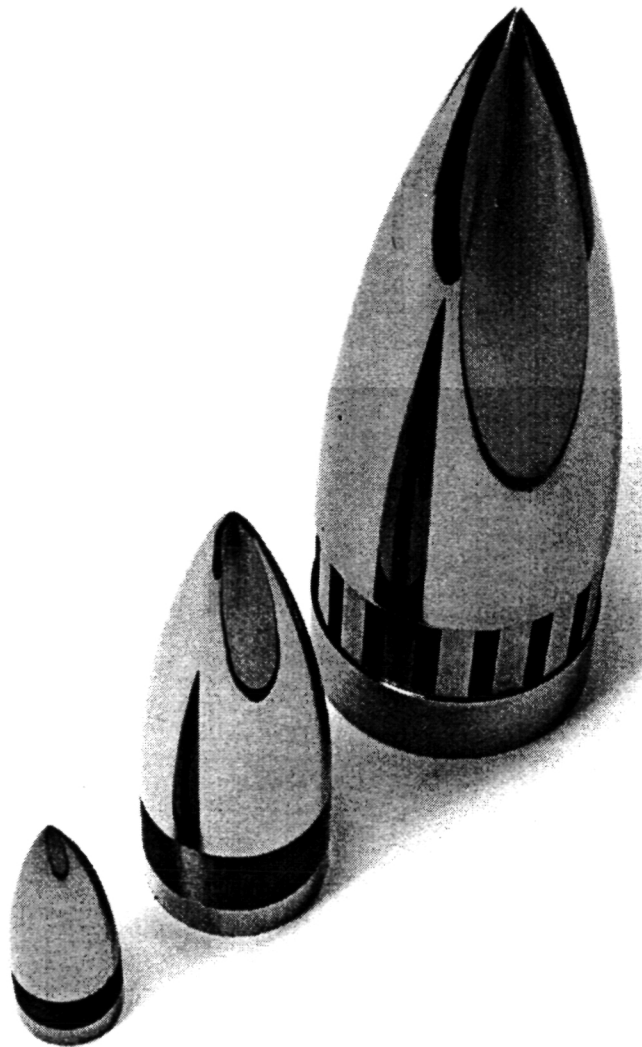


**Figure 3.** 0.5 inch and 1.0 inch B&K in-flow microphones and the 1.5 inch model (no screen).

The model's interior design was different for surface pressure measurements and for boundary layer velocity and cavity acoustic measurements. The primary difference was a drilled-through insert used in the former case, which allows the passage of pressure tubing to outside transducers and instruments. In all other measurements, the standard forward cavity wall similar to the B&K in-flow microphones was used.

### **2.3 Model Mounting and Alignment**

Throughout the experiment, the 1.5 inch microphone model was mounted on a vertical McMasters-Henderson<sup>\*</sup> airfoil strut. This set-up, together with the two-axis hot-wire traverse, was mounted on a pedestal, which in turn was mounted on a large 18 ft. traverse on the floor. As a result, the entire model/traverse assembly, displayed in figure 4, could be easily moved to different stations along the jet longitudinal axis.

The jet-to-model cross-sectional area ratio was about 22. The microphone cavity was positioned at 1.2 jet diameters downstream of the jet exit plane, well inside the jet potential core. The cavity was located 10 model diameters upstream of the vertical strut to reduce the strut's interference effect. In each measurement, the model was carefully aligned with the jet flow by continuously adjusting its orientation until the readings of the four pressure ports, all located at the same longitudinal station ( $X_j/D_j = 1.6$ ) but spaced azimuthally at 90° increments, became the same.

---

<sup>\*</sup> Similar to the NACA 0030 airfoil. (Reference 11.)

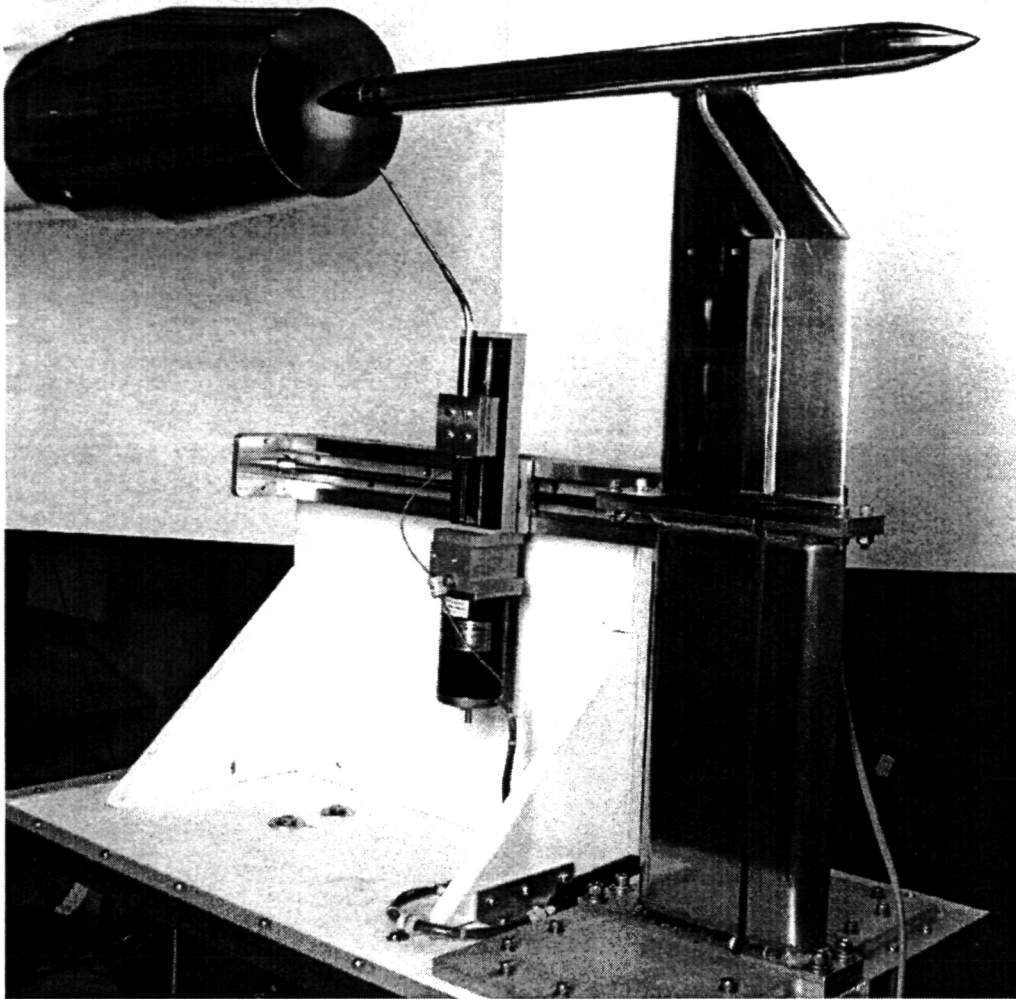


**Figure 4.** Microphone model and traverse assembly.

## **2.4 Surface Pressure Measurements**

Surface pressures over the microphone were measured via seventeen 0.015 inch pressure ports at the longitudinal locations shown in figure 5. The port locations were selected based upon the forebody pressure distribution of a potential flow solution computed numerically with PMARC<sup>\*</sup>. The ports were more densely distributed near the cavity leading edge

---

<sup>\*</sup> Panel Method Ames Research Center (PMARC), a potential flow code developed at NASA Ames Research Center

because of the high pressure gradients in that region. Each port was drilled flush and perpendicular to the local surface. Stainless steel tubing was braised into the ports and extended into the hollow center of the model to connect with Tygon tubing. The Tygon tubing was passed through the central hole of the drilled-through inserts to the support strut and then to a scanning valve and a inclined manometer. The entire length of the tubing was about 6 feet.

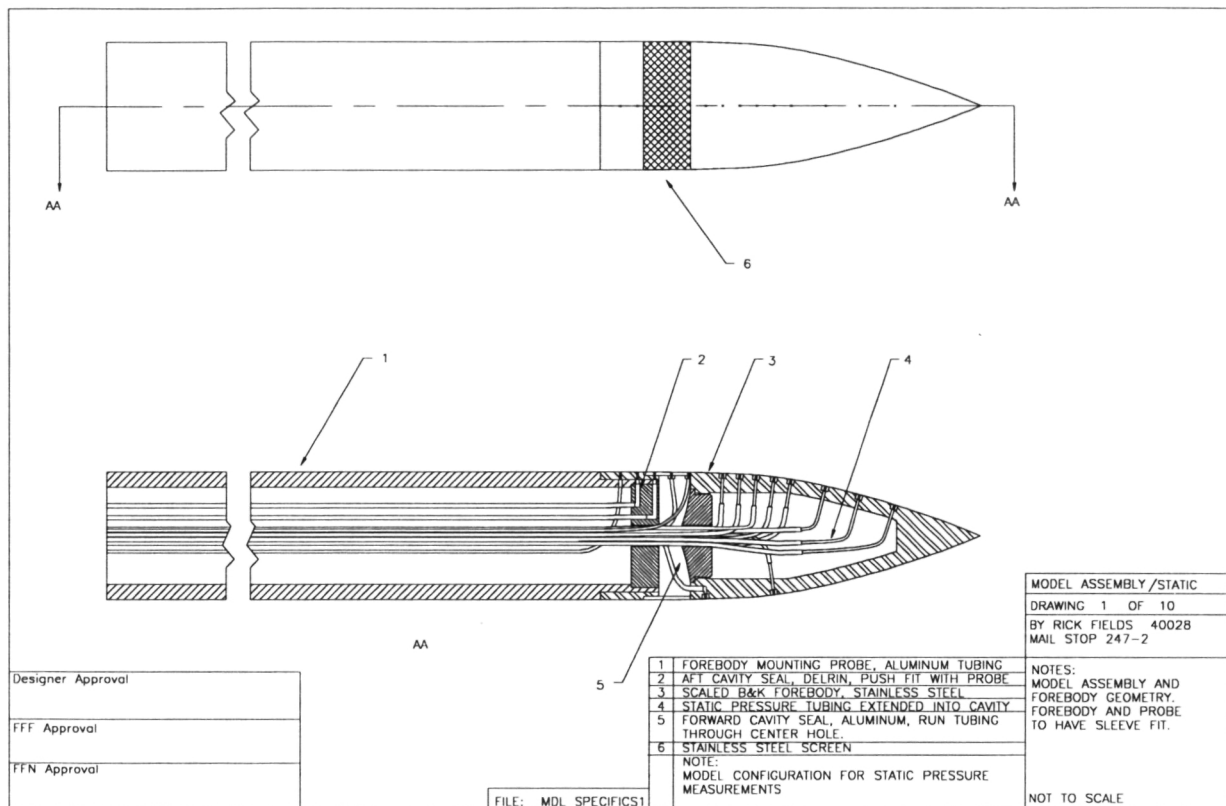


**Figure 5.** Microphone model configured for surface pressure measurements.

## 2.5 Cavity Acoustic Measurements

For all other measurements, the standard forward cavity wall, similar to that of the 0.5 inch B&K UA 0386 microphone, was used. Inside the cavity, a B&K 1 inch 4131 microphone

and 2613 cathode follower, with a flat frequency response from 2-20 kHz, were placed in the center like the 0.5 inch B&K in-flow microphone. The microphone was held in place with a threaded Delrin insert and two electrical isolators, as shown in figure 6. It was connected with a microphone cable through the support probe and vertical strut to a B&K 2639 pre-amplifier. A separate 1/4 inch B&K 4133 microphone together with a B&K 2639 cathode follower was used for far field measurements in the anechoic chamber.

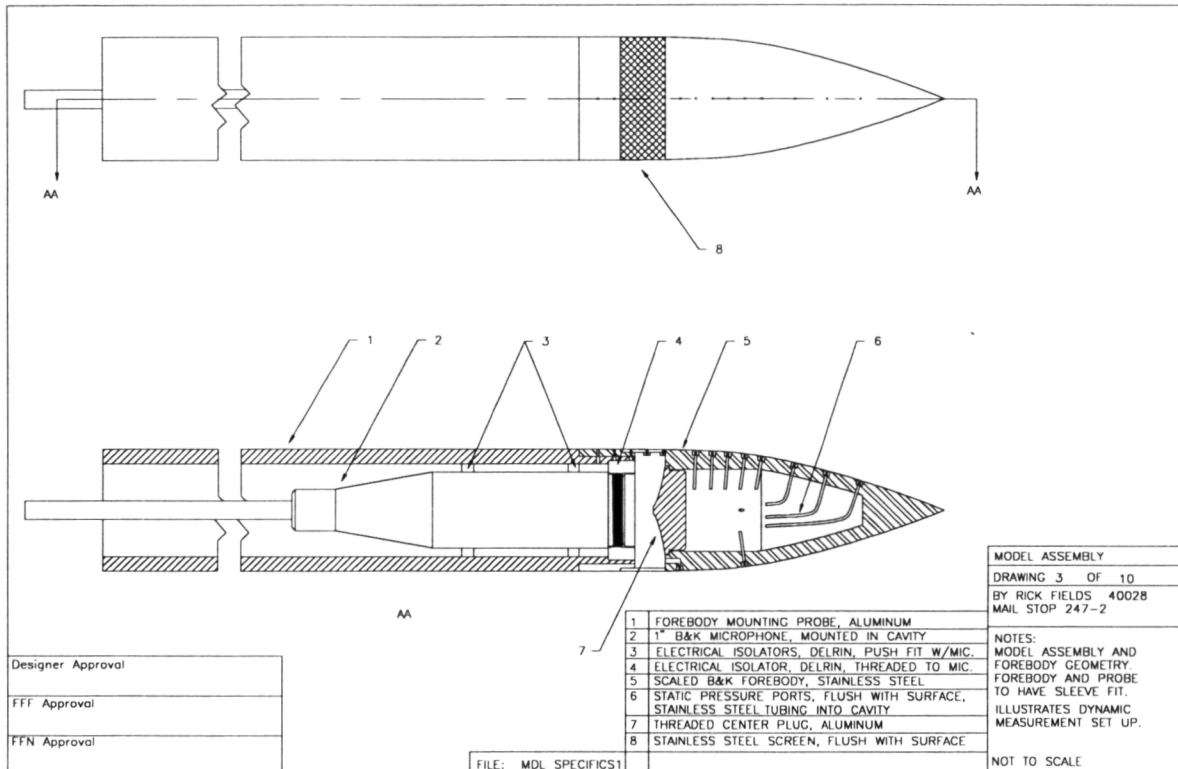


**Figure 6.** Microphone model configured for acoustic measurements.

## 2.6 Boundary-Layer Velocity Profiles

The boundary-layer velocity profiles over the microphone forebody and cavity screen were measured with a DISA 55P26 5 $\mu$ m platinum-tungsten single hot-wire probe. The hot-wire was mounted on a two-axis, linear traverse that could move in directions parallel and

perpendicular to the jet longitudinal axis. The traverse was driven with a Compumotor LN57-102 low-noise stepping motor, which was controlled remotely by a Compumotor 4000 controller. The hot-wire was connected to a DISA 55M01 constant temperature anemometer, followed by a DISA 55D26 linearizer and a DISA 55D10 signal conditioner. The output signals were later transmitted to an HP 3562A spectrum analyzer and an HP 5401A digital oscilloscope for analysis and display. Meanwhile, the signals were recorded with a TEAC RD 120T PCM Data Recorder for post-processing. The same display and recording instruments were also used for acoustic measurements. See figure 7 for the overall instrumentation flow chart.

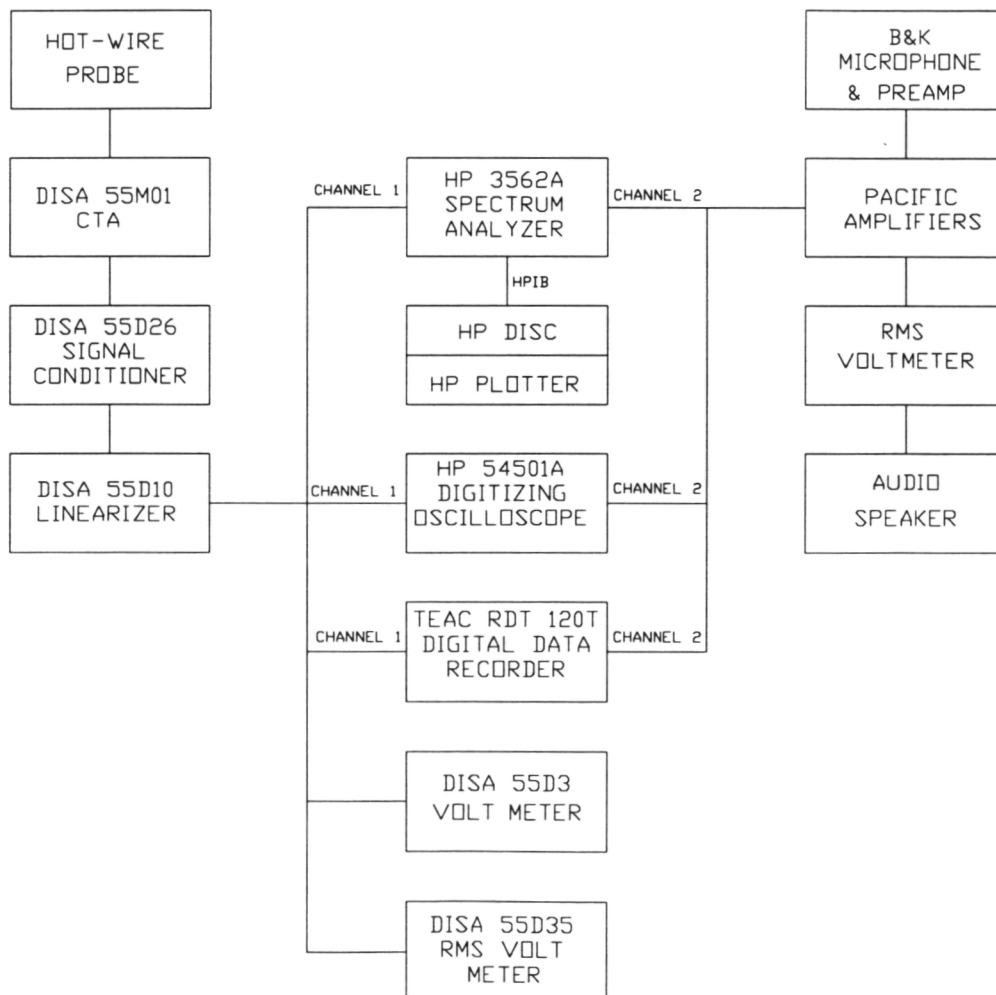


**Figure 7.** Instrumentation flow chart.

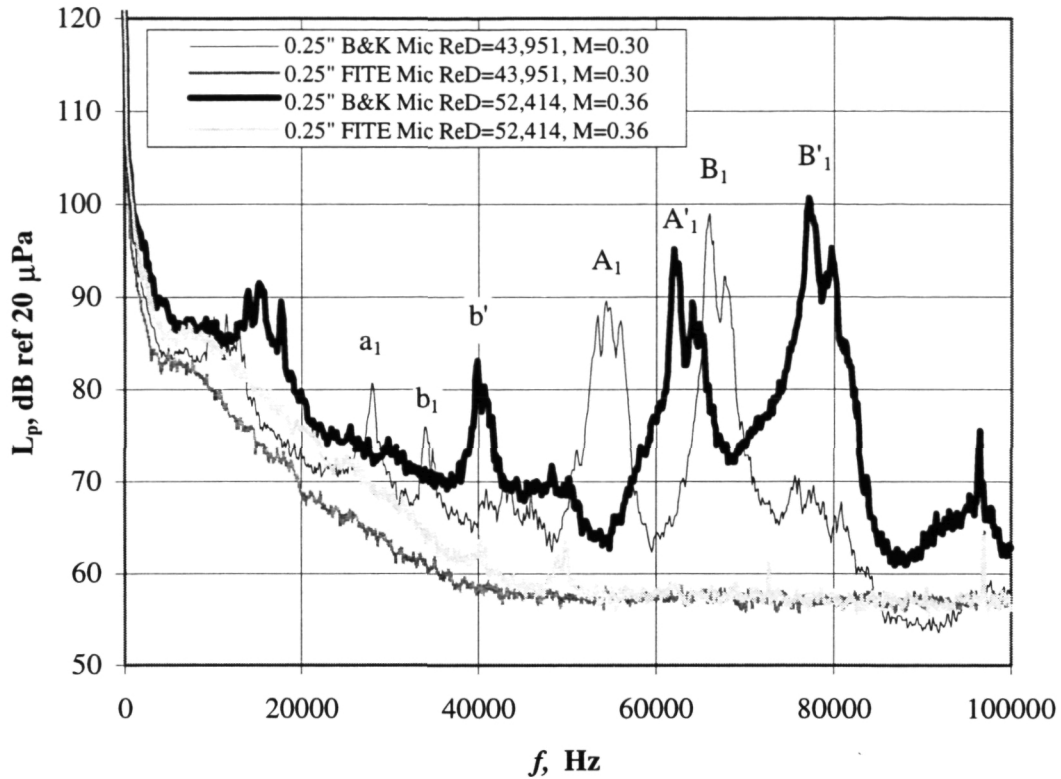
### **3. RESULTS AND DISCUSSION**

#### **3.1 A Comparison of the B&K and FITE Microphones**

One early concern with this investigation was whether the 1.5 inch microphone model can duplicate the cavity oscillations observed on the B&K microphones. To verify this, the model's acoustic spectra were measured and compared with previous wind tunnel data of two B&K microphones obtained by Allen and Soderman<sup>3</sup> at NASA Ames. Since their measurements were made to compare the B&K and FITE microphones, the FITE's data are also included for comparison.

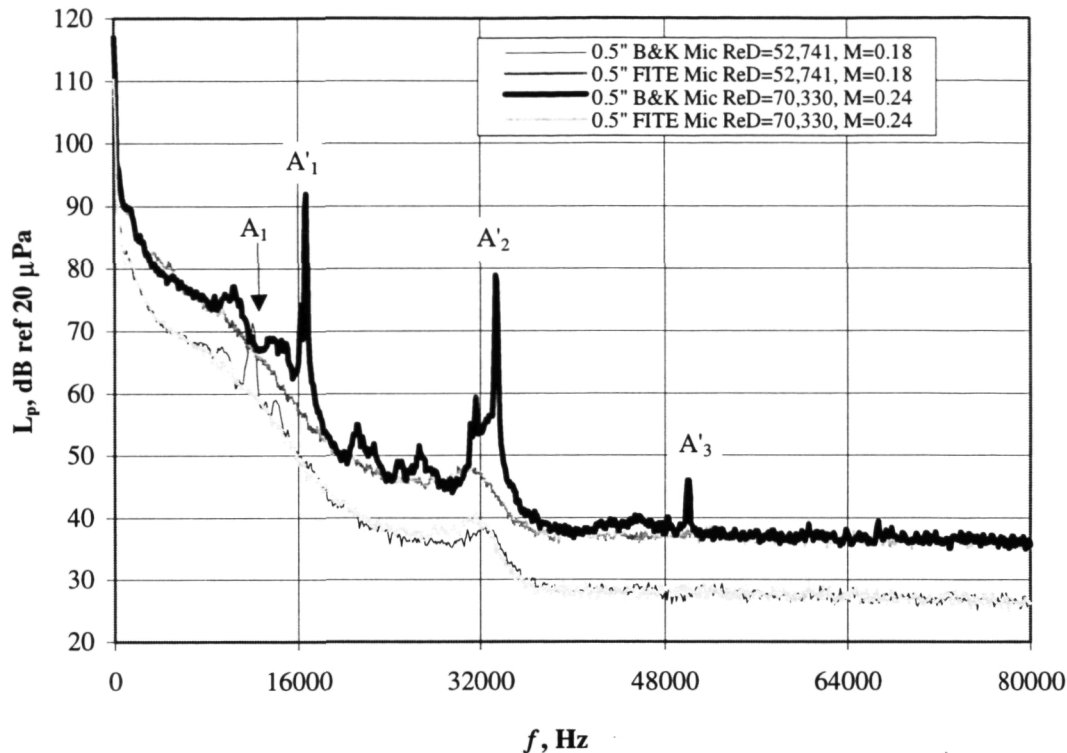
##### **3.1.1 0.25 inch and 0.5 inch B&K microphones**

Figure 8 shows the acoustic power spectra of a 0.25 inch B&K UA 0385 microphone and a corresponding FITE microphone of the same diameter and cavity geometry at two Reynolds numbers. The measurements were made simultaneously in the NASA Ames 40- by 80- Foot Wind Tunnel. As seen in the figure, at  $Re_D = 43,951$ , the B&K microphone has two acoustic tones at 54 ( $A_1$ ) and 64 ( $B_1$ ) kHz, respectively. These tones are 20-40 dB over the wind tunnel noise floor; they are accompanied by respective subharmonics at 27 ( $a_1$ ) and 32 ( $b_1$ ) kHz. The FITE's spectrum on the other hand does not show such acoustic oscillations. As the Reynolds number is increased to 52,414, both the B&K fundamental and subharmonic oscillations increase in frequency and magnitude. The FITE's spectrum at this higher Reynolds number again shows no observable acoustic oscillations.



**Figure 8.** Acoustic power spectra of 0.25 inch B&K and FITE microphones measured in the NASA Ames 40- by 80- Foot Wind Tunnel:  $A_1$ ,  $B_1$  = dominant tones at  $Re_D = 43,951$ ;  $a_1$ ,  $b_1$  = subharmonics of  $A_1$  and  $B_1$ ;  $A'_1$ ,  $B'_1$  = dominant tones at  $Re_D = 52,414$ ;  $b'_1$  = subharmonic of  $B'_1$ . (Reference 3.)

A similar comparison is shown in figure 9 for a 0.5 inch B&K UA 0386 microphone and a 0.5 inch FITE microphone tested simultaneously in the NASA Ames 7- by 10- Foot Wind Tunnel. At  $Re_D = 52,741$  the 0.5 inch B&K microphone has a weak tone at 12.5 kHz ( $A_1$ ). As the Reynolds number is increased to 70,330, the noise floor increases for both the B&K and FITE microphones. The B&K spectrum shows a strong peak at 16.7 kHz ( $A'_1$ ), more than 30 dB above the noise floor, and it is accompanied by harmonics at 33.4 and 50.1 kHz. For both Reynolds numbers, the FITE spectra shows no noticeable acoustic oscillations.



**Figure 9.** Acoustic power spectra of 0.5 inch B&K and FITE microphones measured in the NASA Ames 7- by 10- Foot Wind Tunnel:  $A_1$  = dominant tone at  $Re_D = 52,741$ ;  $A'_1$  = dominant tone at  $Re_D = 70,330$ ;  $A'_2$  and  $A'_3$  = second and third harmonics of  $A_1$ . (Reference 3.)

### 3.1.2 The 1.5 inch B&K microphone model

The trends observed on the B&K microphones were also seen on the 1.5 inch B&K microphone model. Figure 10 shows the acoustic power spectra of the 1.5 inch model measured in the Anechoic Chamber Free-Jet Facility at NASA Ames at three Reynolds numbers. Like the smaller B&K microphones, the 1.5 inch B&K microphone also shows distinct acoustic oscillations. At an initial Reynolds number of 78,000, a strong oscillation is observed at 3.7 kHz ( $A_1$ ). This oscillation is accompanied by two weaker harmonics at 7.4 and 11.1 kHz, respectively. When the Reynolds number is raised to 94,000, the spectrum

shows a dominant oscillation at about 4.5 kHz ( $A'_1$ ), along with two harmonics at 9 and 13.5 kHz, respectively. When the Reynolds number is further increased to 110,000, the dominant oscillation frequency increase to 5.3 ( $A''_1$ ) kHz, and the harmonics to 10.6 and 15.9 kHz. Along with the increased Reynolds number, large magnitude increases are also seen in the spectral peaks and the noise floor.

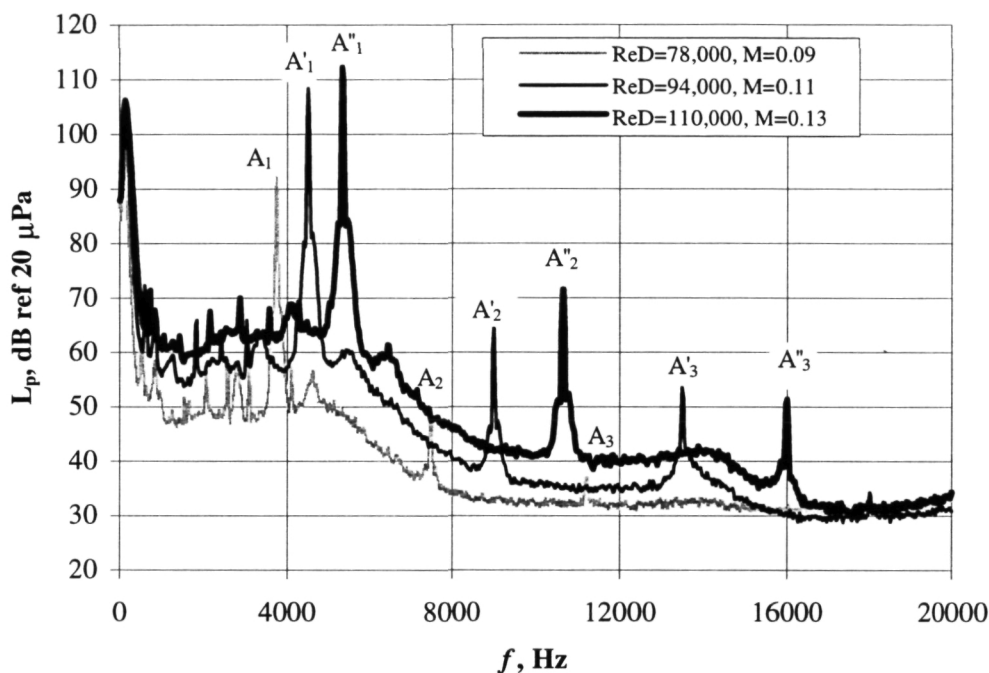


**Figure 10.** Acoustic power spectra of the 1.5 inch B&K microphone model:  $A_1$ ,  $A'_1$ , and  $A''_1$  = dominant tones at  $Re_D = 78,000$ ,  $94,000$ , and  $110,000$ , respectively;  $A_2$  and  $A_3$  = second and third harmonics of  $A_1$ ;  $A'_2$  and  $A'_3$  = second and third harmonics of  $A'_1$ ;  $A''_2$  and  $A''_3$  = second and third harmonics of  $A''_1$ .

### 3.1.3 Strouhal numbers of microphone oscillations

Figure 11 shows the plot of the Strouhal Number of the dominant acoustic oscillations versus Mach number for the 1.5 inch model. The Strouhal number,  $St$  ( $\equiv fL/U_\infty$ ), is defined as the oscillation frequency  $f$ , non-dimensionalized by the cavity length  $L$  and the free stream

velocity  $U_\infty$ . As seen in the figure, the Strouhal number remains constant at 1.35 with the increasing Mach number until  $M = 0.13$ , where it drops to 1.15, indicating a mode change. This trend is reversed as the Mach number is decreased except that a hysteresis occurs near  $M = 0.125$ .

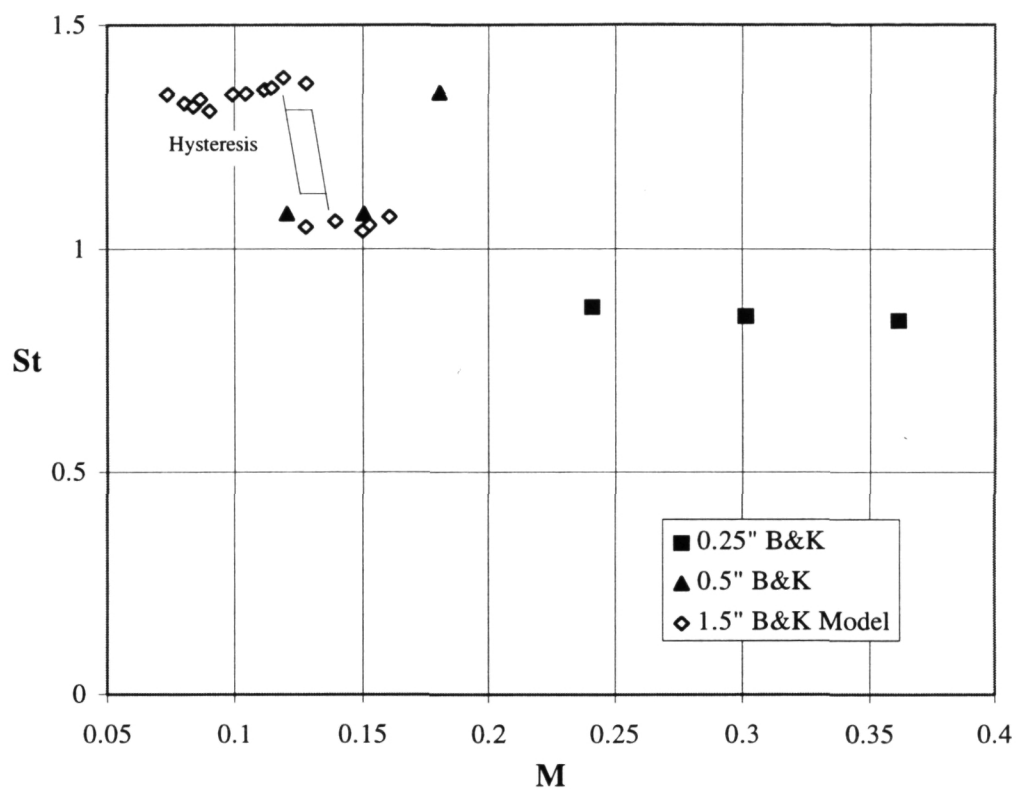


**Figure 11.** Strouhal number vs. Mach number for three B&K in-flow microphones.

Figure 11 also includes the Strouhal numbers of the 0.25 inch and 0.5 inch B&K microphones calculated from Allen and Soderman's spectral data. Though not many, the Strouhal numbers of the 0.5 inch microphone are very close to those of the 1.5 inch microphone, indicating the occurrence of similar cavity acoustic oscillations. Their Strouhal numbers however change at different Mach numbers. The Strouhal numbers of the 0.25 inch

B&K microphone, at about 0.85, are lower than those of the 0.5 inch microphone. They however are still within the experimental uncertainty of the Strouhal numbers of a rectangular cavity measured for instance by Block<sup>5</sup> and Ethembabaoglu<sup>12</sup>. In fact, it was surprising to see that all the microphone Strouhal numbers are fairly close to the Strouhal numbers reported by them. This might have already suggested that they have similar cavity oscillation mechanisms.

The differences among microphone Strouhal numbers could be attributed to their apparently different cavity and orifice geometries. The 0.25 inch B&K microphone has round orifices whereas those of the 0.5 inch and 1.5 inch microphones are rectangular. In addition, the 0.25 inch B&K microphone's internal cavity geometry is markedly different from those of the 0.5 inch and 1.5 inch microphones. Similarly, when comparing a FITE microphone with a B&K microphone, the FITE's forebody is three times longer; its cavity leading edge is located at  $X/D = 6.0$ , as compared to  $X/D = 2.04$  of the B&K microphone. It has a round, blunt nose, sharply different from the pointed apex of the B&K microphone. Again, one could attribute the success of the FITE microphone to its apparently different forebody geometry.

But as previous cavity oscillation studies<sup>7,8</sup> have shown, the differences are perhaps more related to the conditions at the flow separation point, the cavity leading edge, which we do not have. As a result, an extensive flow survey was conducted over the microphone forebody and cavity screen of the 1.5 inch model in order to understand its cavity acoustic oscillation mechanisms.

### 3.2 Mean Flow Measurements

#### 3.2.1 Surface pressure measurements

The microphone forebody's geometry and cavity location determine its surface pressure distribution. Actually, because of the apparent geometry differences between the FITE and B&K microphones, it had one time been suspected by Allen that the pressure gradient near the cavity of the B&K microphone is somehow responsible for the observed cavity acoustic oscillations. Such thinking had been supported by Meyer, Mechel and Kurtze's<sup>13</sup> observation that freestream acoustic pressure should be measured far downstream of any region with significant pressure gradients. As a result, surface pressure was the first flow property measured over the forebody surface of the 1.5 inch B&K microphone model. It has also been computed numerically with PMARC for comparison.

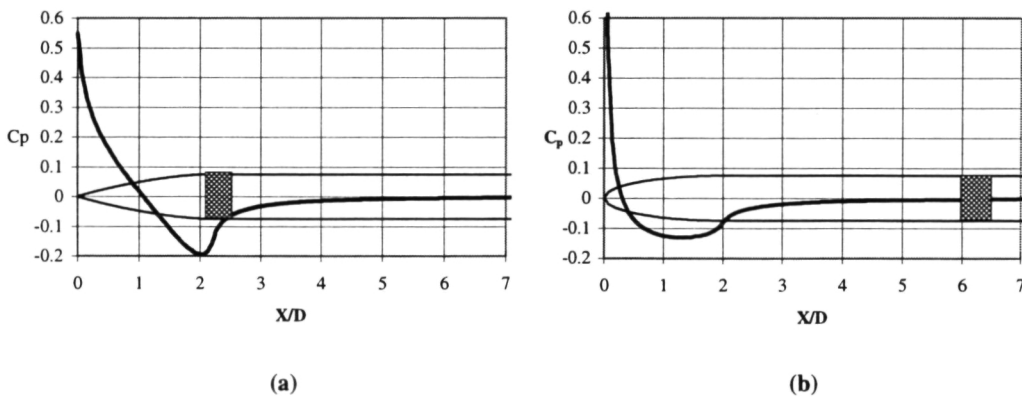


**Figure 12.** Surface pressure distributions obtained by PMARC over (a) the B&K microphone, and (b) the FITE microphone.

Figure 12 shows the pressure distributions computed for the B&K and FITE microphones. Since PMARC uses a panel method, it cannot model the microphone screen and cavity; only the solid body models, with no cavities, were computed. The figure shows that the cavity of the B&K microphone is located in the most severe pressure gradient region. As figure 12(a)

shows, the B&K pressure distribution has a moderate negative gradient, extending all the way up to  $X/D=2.0$ . Beyond this point, a strong adverse pressure gradient appears over the cavity, and the pressure recovery is not complete until about  $X/D=5$ . In contrast, figure 12(b) shows that the severity of the adverse pressure gradient is much less in the FITE's pressure distribution because of its long forebody length following its blunt nose. For the FITE, the cavity leading edge is located at  $X/D=6.0$ , well downstream of the adverse pressure gradient region.

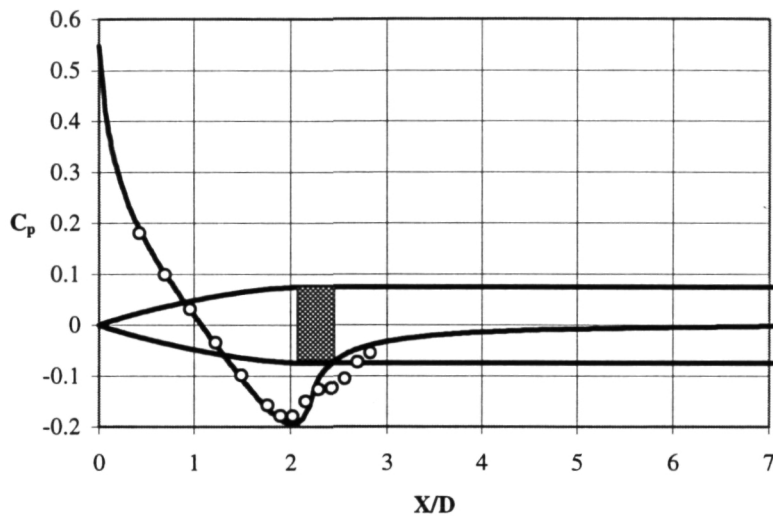


**Figure 13.** Surface pressure distribution measured over the 1.5 inch B&K microphone model.

The measured pressure distribution over the B&K forebody model is shown in figure 13. During the experiment, tones were audible from the wind tunnel sideline. Because of the Tygon tubing passing through the cavity, however, no acoustic measurements were made. As seen in the figure, the measured pressure distribution compares well with the numerical solution near the nose cone. They start deviating in the vicinity of the screen. Unlike the

numerical solution, the measured pressure distribution has an apparent plateau across the screen and it does not recover until farther downstream of the cavity.

### 3.2.2 Mean velocity distributions

Following surface pressures, streamwise velocities were measured for cases with and without the microphone cavity. This was done by traversing a single hot-wire probe across boundary layers at successive longitudinal stations. In the case without the cavity, the cavity was simply replaced by a solid cylinder of the same diameter. It was only done at  $Re_D = 110,000$  in order to study instabilities in the forebody boundary layer without interference from the cavity.

Figure 14 shows the velocity profiles of the 1.5 inch microphone model without the cavity. It shows that the boundary layer thickness increases continuously, starting at 0.020 inch at the foremost station and increased to 0.037 inch at the last station. The boundary layer is laminar as the shape factors of all these profiles fall in a range from 2.2-2.5.<sup>14</sup> However, inflection points are seen in the profiles at the last few stations; it means that boundary layer instabilities have grown to a finite amplitude near the cavity trailing edge location. This is consistent with Arakeri's<sup>15</sup> study.

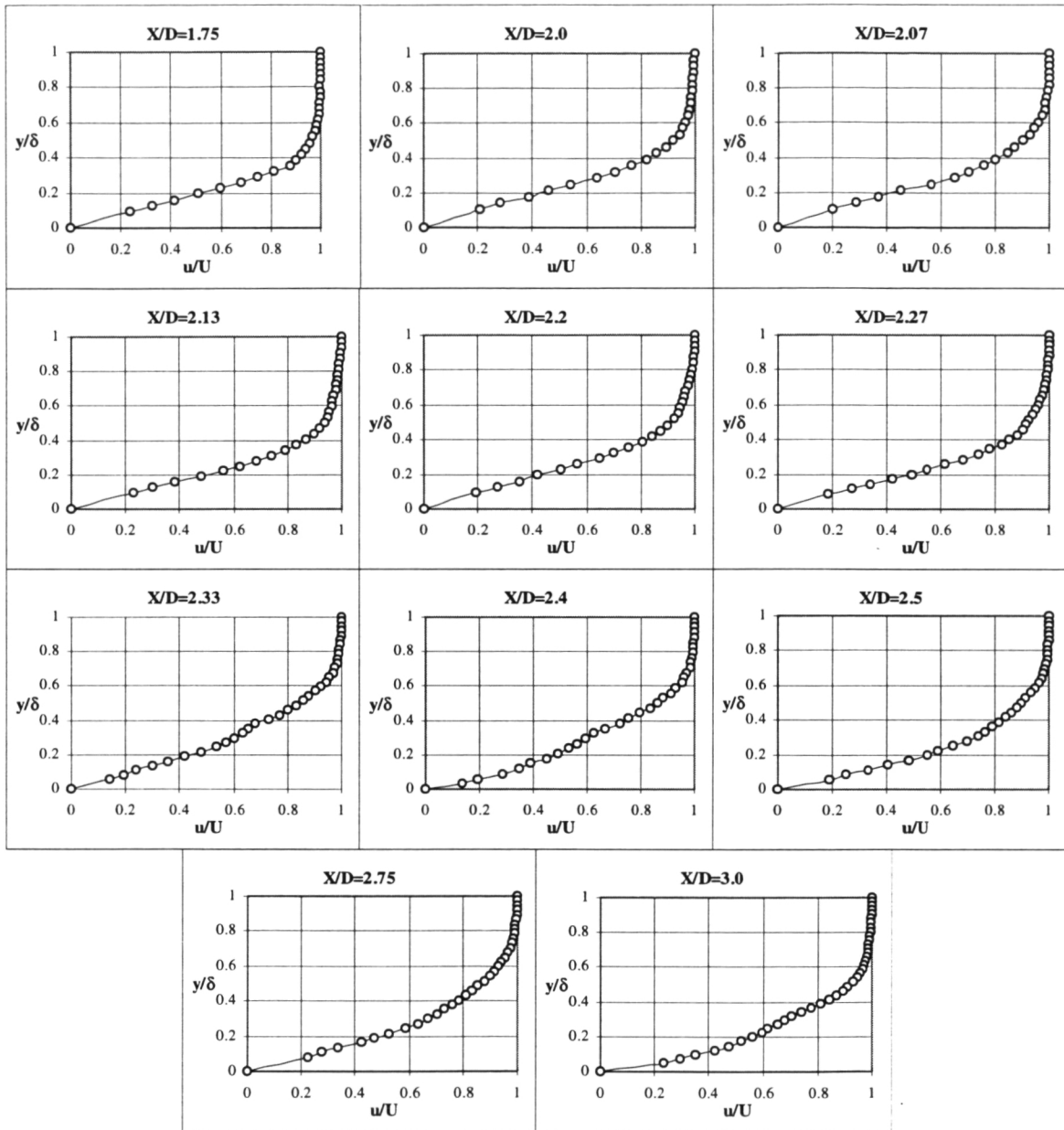


**Figure 14.** Streamwise evolution of mean velocity profiles over the model with no cavity at  $Re_D = 110,000$ .

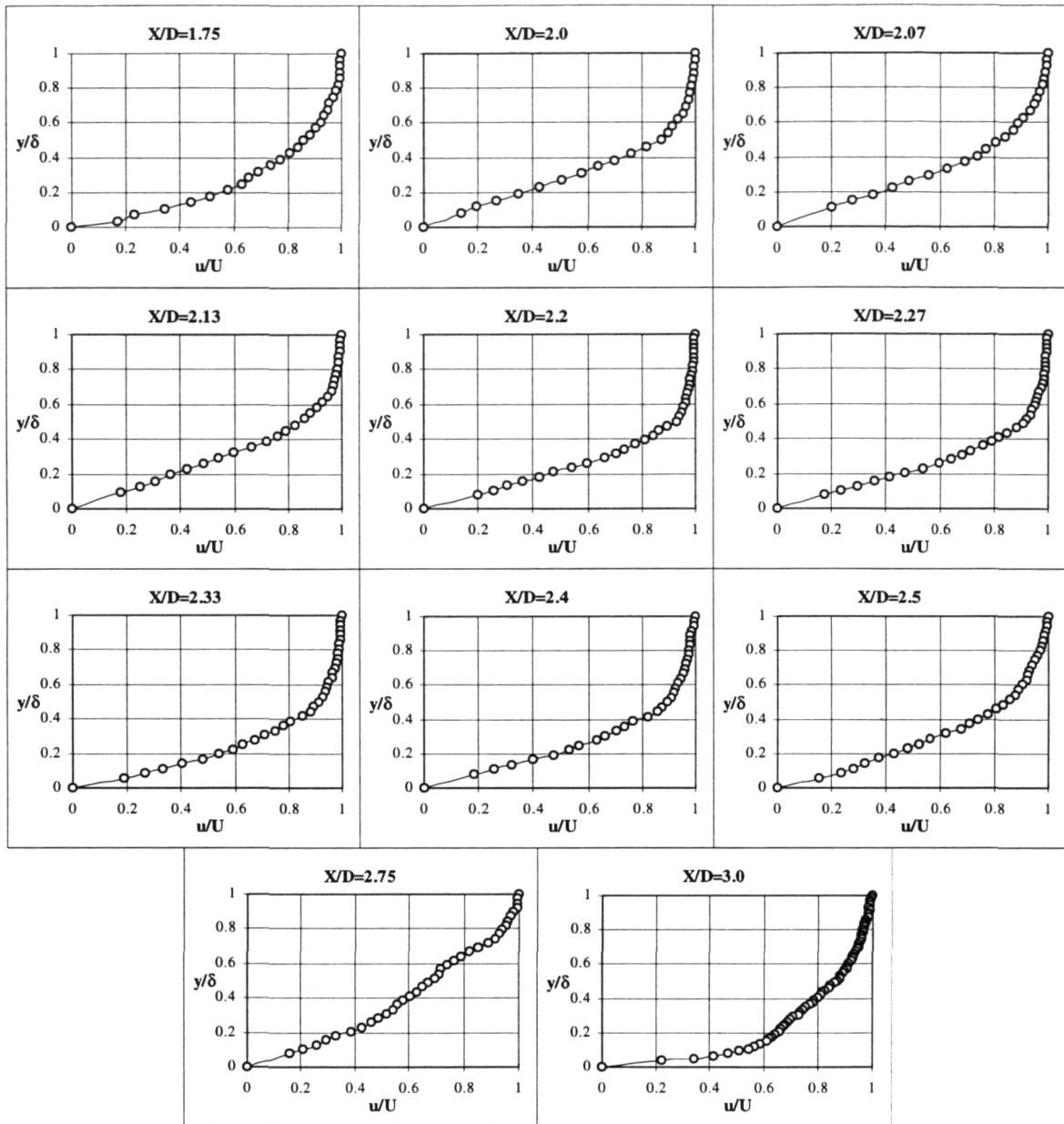


**Figure 15.** Streamwise evolution of mean velocity profiles over the model with cavity at  $Re_D = 78,000$ .

Figures 15-17 display the velocity profiles for the case with the cavity at  $Re_D = 78,000$ , 94,000 and 110,000, respectively. As seen in figure 15, the shape factors of these profiles are around 2.5, indicating a laminar boundary layer. However, in the vicinity of the cavity trailing edge ( $X/D=2.35$ ), there is an inflection point in the velocity profile and a sudden

increase in boundary layer thickness. The boundary layer, when compared to the case with no cavity, shows a rapid growth from 0.021 inch at  $X/D=1.75$  to about 0.070 inch at  $X/D=3.0$ . This could be due to an upwash from inside the cavity or a vortex in that region.

The features at  $Re_D = 94,000$  are largely the same, as shown in figure 16.

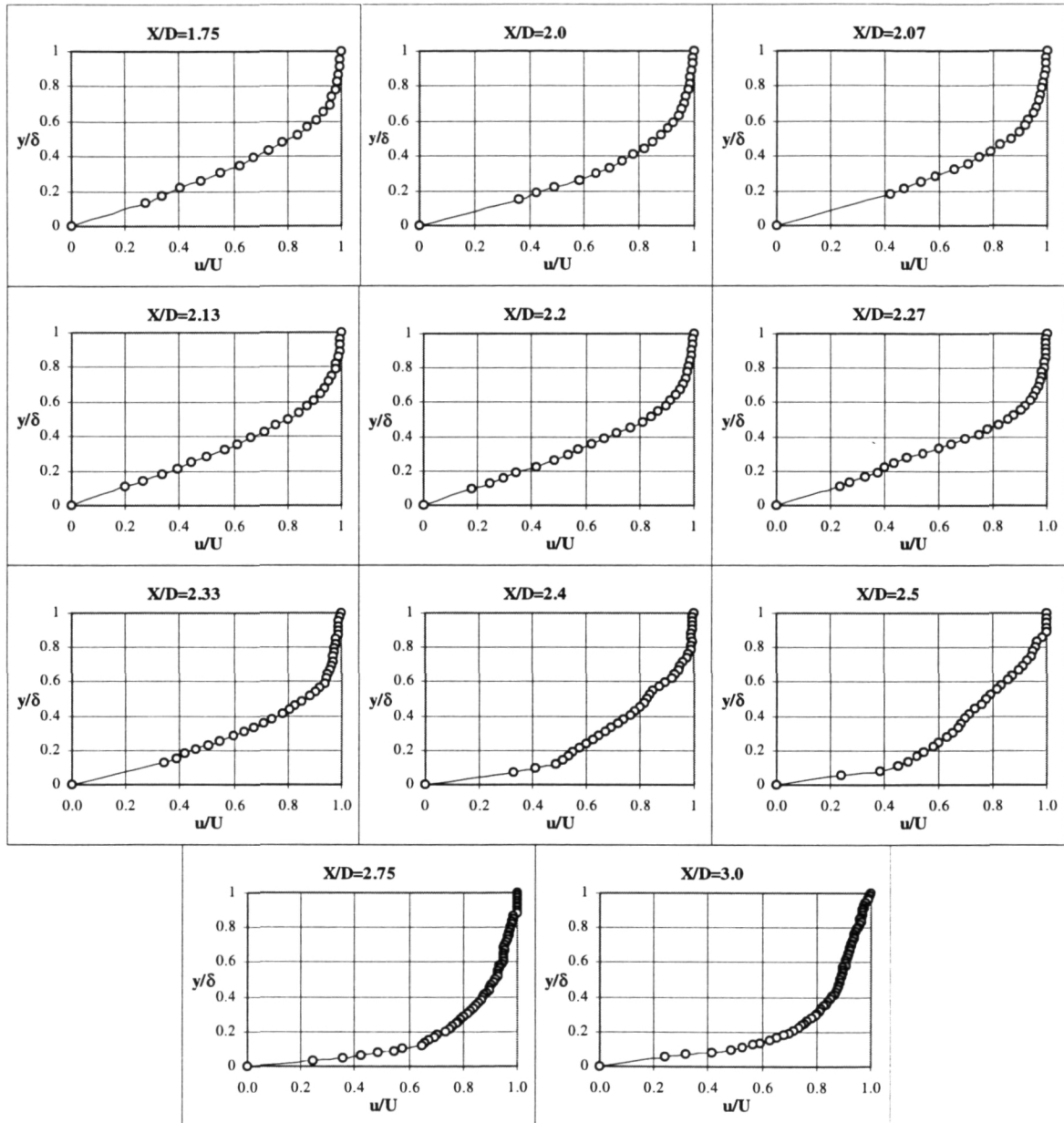


**Figure 16.** Streamwise evolution of mean velocity profiles over the model with cavity at  $Re_D = 94,000$ .

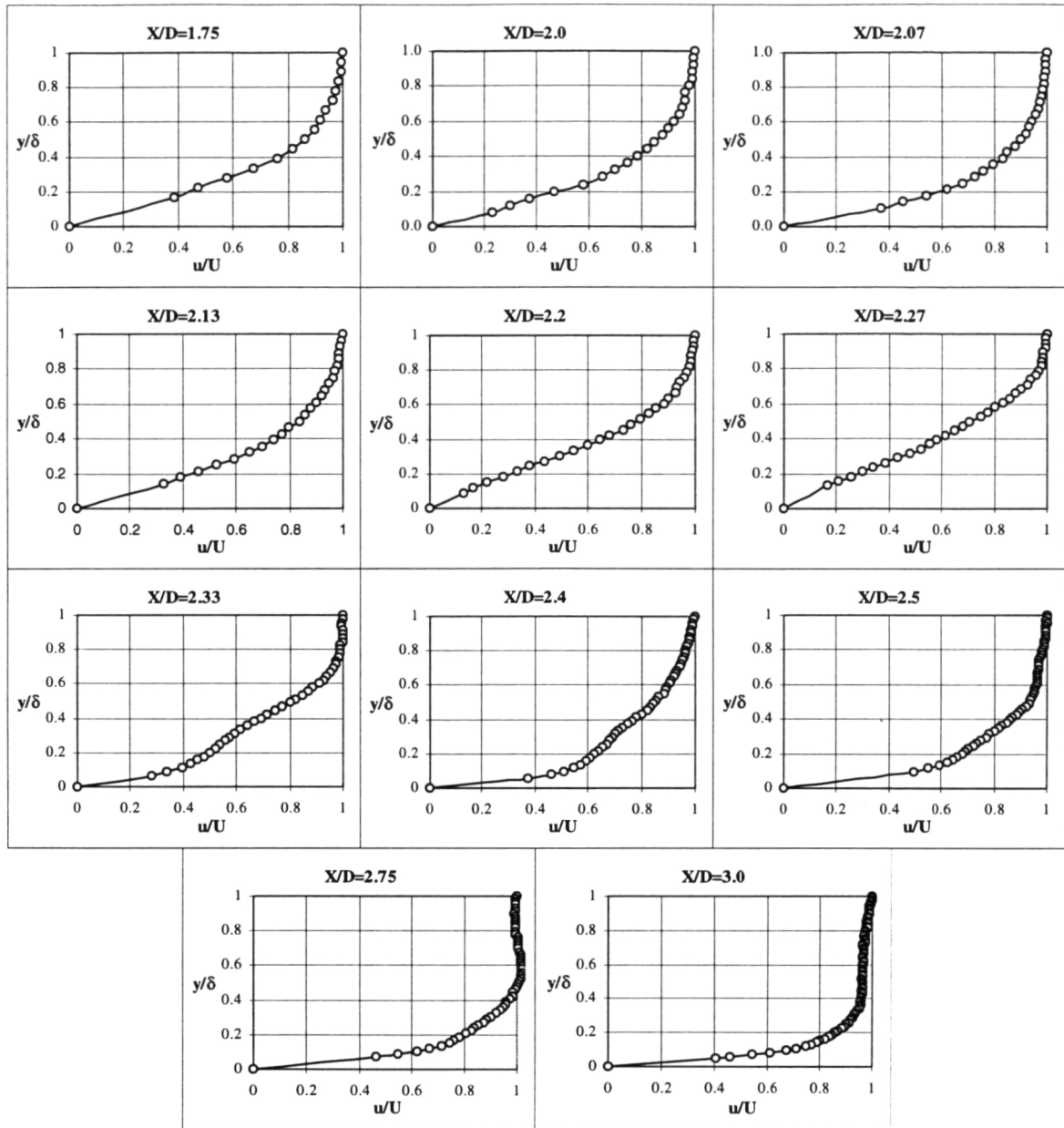


**Figure 17.** Streamwise evolution of mean velocity profiles over the model with cavity at  $Re_D = 110,000$ .

At the highest Reynolds number  $Re_D = 110,000$ , the boundary layer begins to develop a fuller profile in the vicinity of the cavity trailing edge, as shown in figure 17. Its thickness experiences a rapid increase, and its shape factor decreases from 2.5 at the cavity leading

edge to 1.6 at  $X/D=3.0$ . All these results suggest that the flow becomes more turbulent over the cavity at this high Reynolds number.<sup>14</sup> This is different from the mean velocity profile of the solid model shown in figure 14, which shows that the boundary layer is laminar but unstable, with an inflection point near the cavity trailing edge. Again, when compared to the case with no cavity, the rapid boundary layer growth near the trailing edge indicates that the cavity flow is strong enough to modify the mean velocity profiles as suggested by Rockwell and Naudascher<sup>8</sup>.

### **3.2.3 Velocity disturbance intensity**

Figure 18 shows the profiles of velocity disturbance intensity over the microphone model without a cavity. The figure shows that velocity disturbances grow with the increased longitudinal distance like in a normal boundary layer; the maximum disturbance intensity is about 2%. Similar profiles for the case with a cavity are shown in figures 19-20 for Reynolds numbers 98,000 and 110,000. As seen in the figures, up to the leading edge of the cavity, the disturbance intensity profiles compare well with the case with no cavity. However, the intensity grows rapidly across the screen, and reaches a maximum at  $X/D=2.4-2.5$ , in the vicinity of the cavity trailing edge. The maximum disturbance intensity there is about 17-19%, which is an order-of-magnitude higher than the case with no cavity. This is consistent with the inflection points seen in the mean velocity profiles in the same region - both suggest that some strong cavity flow disturbances occur near the cavity trailing edge. The disturbances grow slightly beyond the cavity trailing edge, and starts decaying afterwards.

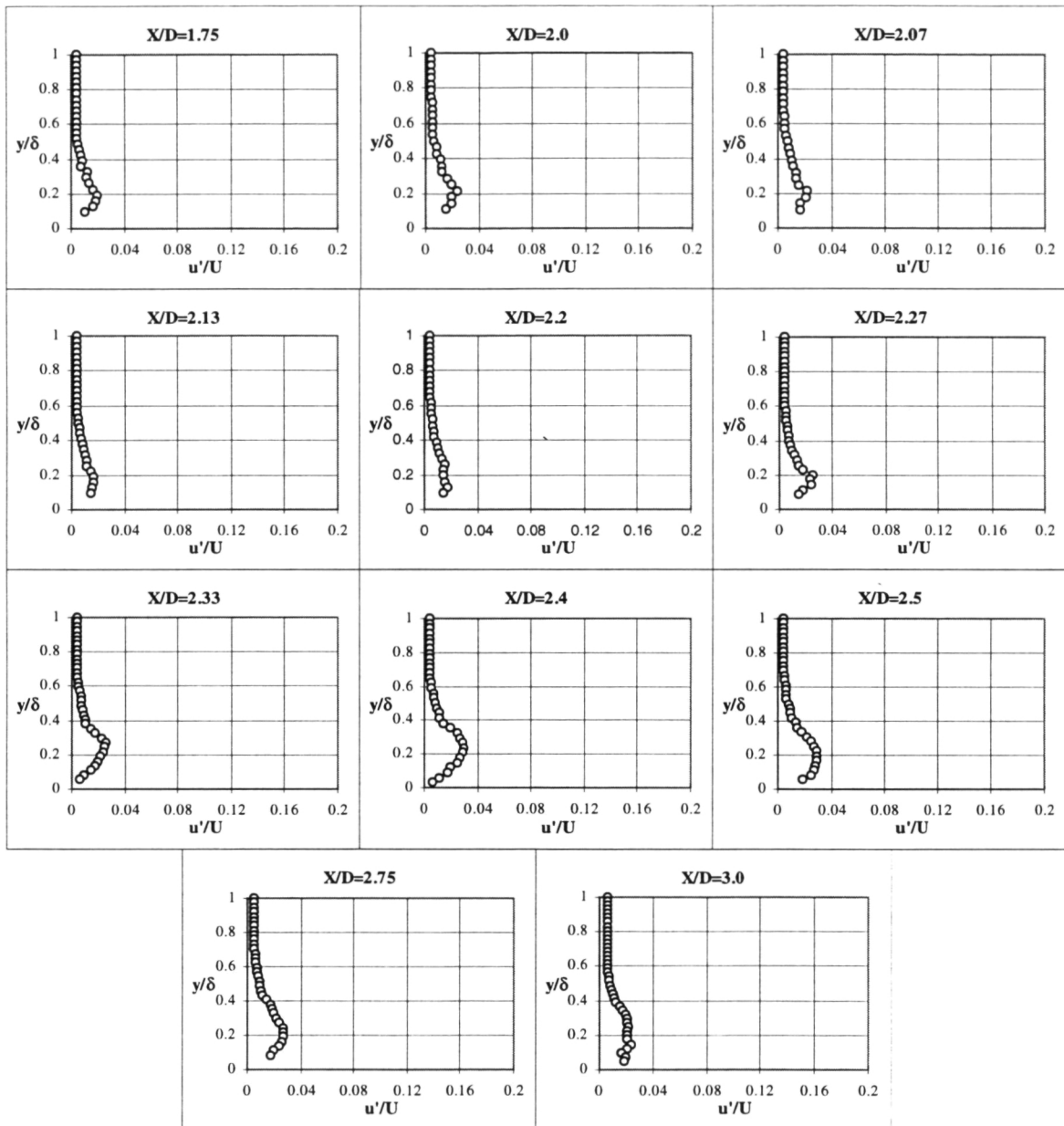


**Figure 18.** Streamwise evolution of velocity disturbance intensity over the model with no cavity at  $Re_D = 110,000$ .

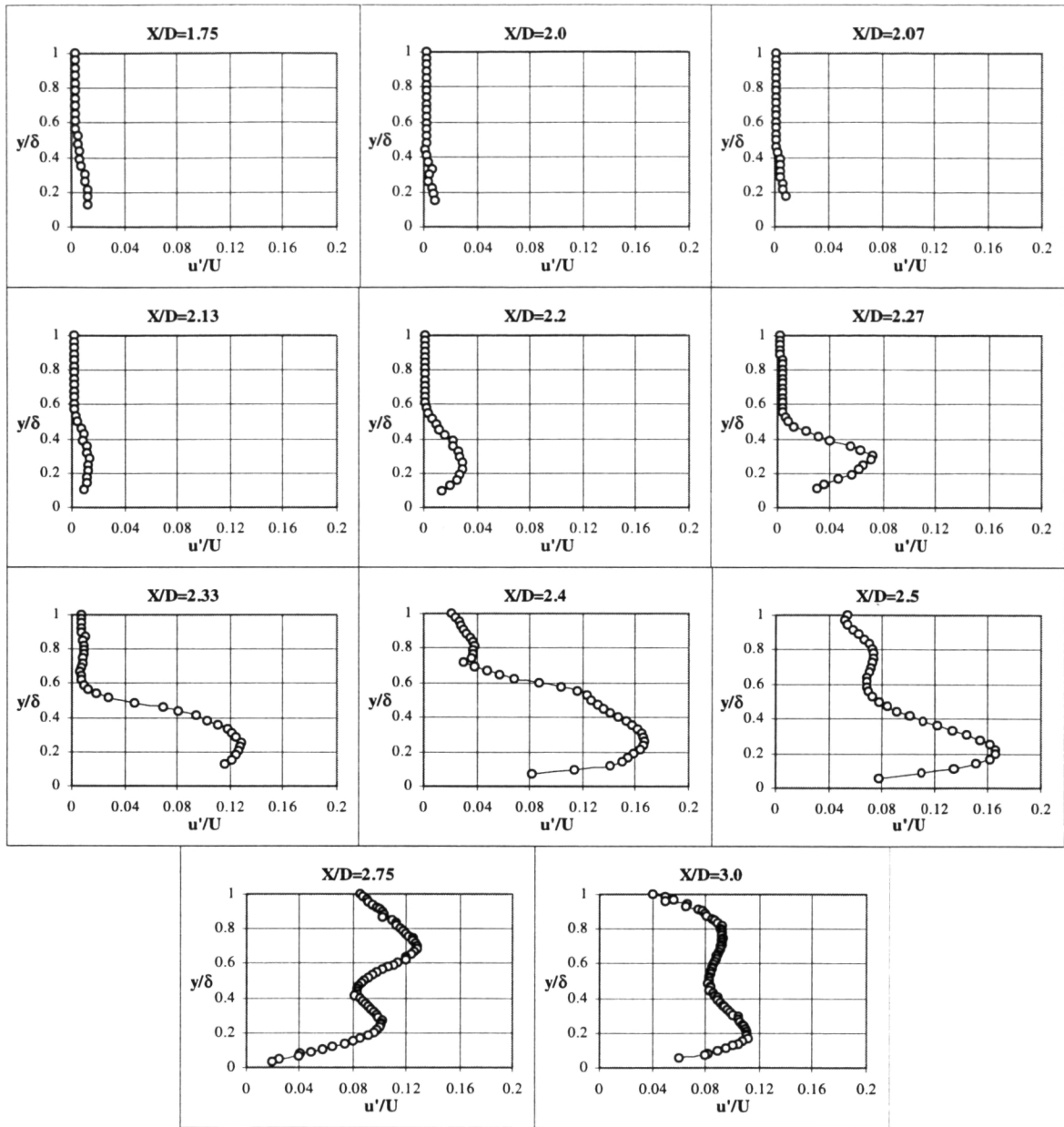


**Figure 19.** Streamwise evolution of velocity disturbance intensity over the model with cavity at  $Re_D = 94,000$ .

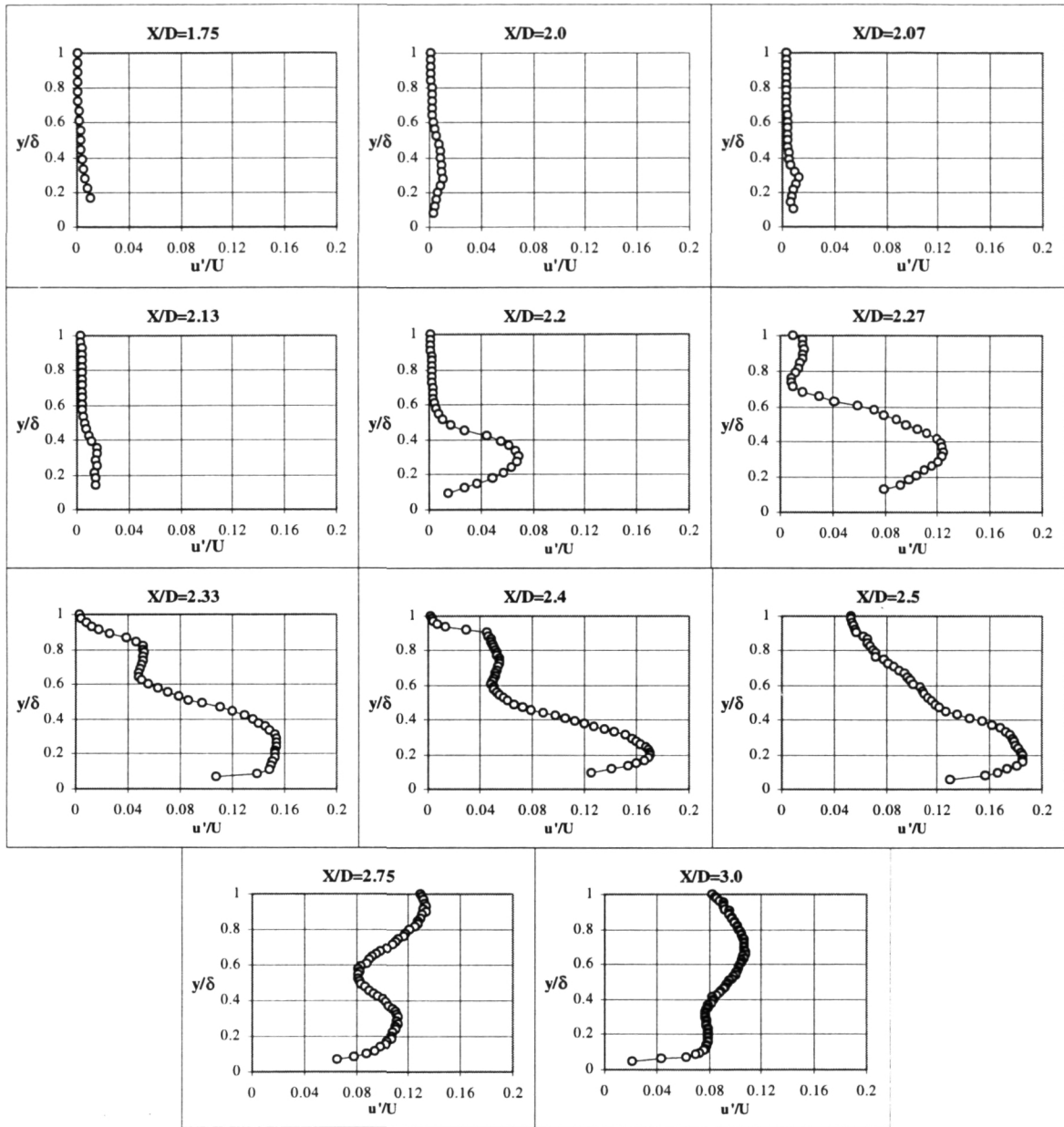


**Figure 20.** Streamwise evolution of velocity disturbance intensity over the model with cavity at  $Re_D = 110,000$ .

### 3.3 Spectral Relationship between Velocity and Acoustic Oscillations

The strong flow disturbances observed at the cavity trailing edge and the Strouhal number comparison in section 3.1.3 together seem to suggest that the phenomenon is caused by cavity shear layer oscillations impinging on the cavity trailing edge, which in turn excites cavity acoustic resonance. In either case, however, coupling between cavity velocity and acoustic oscillations is essential to sustain cavity tones. As a result, these two quantities were measured simultaneously at  $Re_D = 78,000$ ,  $94,000$ , and  $110,000$ , respectively, in order to examine and differentiate the cavity acoustic oscillation mechanisms. The acoustic power spectra have been presented in previous sections. This section will only emphasize the spectral relationship between velocity and acoustic oscillations.

#### 3.3.1 Velocity and acoustic spectra

As before, the velocity power spectra at  $Re_D = 110,000$  for the case with no cavity are included for comparison. This is shown in figure 21. At each station, the hot-wire was positioned at a transverse ( $y$ ) location where the mean velocity was close to  $0.3U_e$  ( $U_e$ , the edge velocity of the boundary layer). For most of the boundary layers surveyed before the cavity trailing edge, the hot-wire position was close to  $y/\delta = 0.2$ ; it was closer to the surface when the boundary layer became more turbulent downstream of the cavity trailing edge. The results show that velocity oscillations are very weak until  $X/D = 2.4-2.5$ , beyond which a broadband excitation between 1-5 kHz is suddenly seen in the power spectra. The spectra increase in both frequency bandwidth and magnitude as the hot-wire moved farther downstream; they suggest that the boundary layer is in transition to turbulence.

Recall that figure 10 shows the acoustic power spectra for all three Reynolds numbers for the case with a cavity. As seen in that figure, at  $Re_D = 78,000$ , the acoustic spectrum has a distinct tone at about 3.6 kHz. The velocity spectrum, shown in figure 22, on the other hand is calm with no noticeable peaks at  $X/D=1.75$ ; it starts to show a spectrum peak at the same frequency at  $X/D=2.07$ , 0.02 inches aft of the cavity leading edge. With increased distance from the cavity leading edge, the spectrum peak, accompanied by increasing harmonics, grows in magnitude until a maximum is reached at  $X/D=2.5$ , near the cavity trailing edge. Afterwards, the spectrum peaks decrease in magnitude and the spectral noise floor rises, indicating a transition to turbulence in the boundary layer. These velocity fluctuations are not, as one would suspect, due to acoustic particle velocities. Actually, by exposing the hot-wire to a 120 dB loudspeaker sound at 4 kHz on the jet centerline, it has been shown that the hot-wire could not resolve the very small acoustic velocity signals.

The velocity spectra at  $Re_D = 94,000$  and  $110,000$ , shown respectively in figures 23 and 24, are largely similar to those at  $Re_D = 78,000$ , except that their spectral peaks have higher frequencies and magnitudes. In addition, in both cases, velocity oscillations can be seen at  $X/D=1.75$ , 0.375 inches forward of the cavity leading edge. As the  $Re_D = 78,000$  case, velocity oscillations are amplified along the cavity screen and reach a maximum at  $X/D=2.33$ , near the cavity trailing edge. Afterwards, the noise floors rise and oscillations diminish, likely due to increased turbulence. Note that for the spectra of the solid model at  $Re_D=110,000$  (figure 21), none of its spectral peaks seem to match the dominant oscillation or its harmonics and subharmonics of the cavity oscillations shown in figure 24. This

suggests that the microphone cavity flow oscillations are caused by mechanisms other than the forebody boundary layer instabilities.

ORIGINAL PAGE  
COLOR PHOTOGRAPH

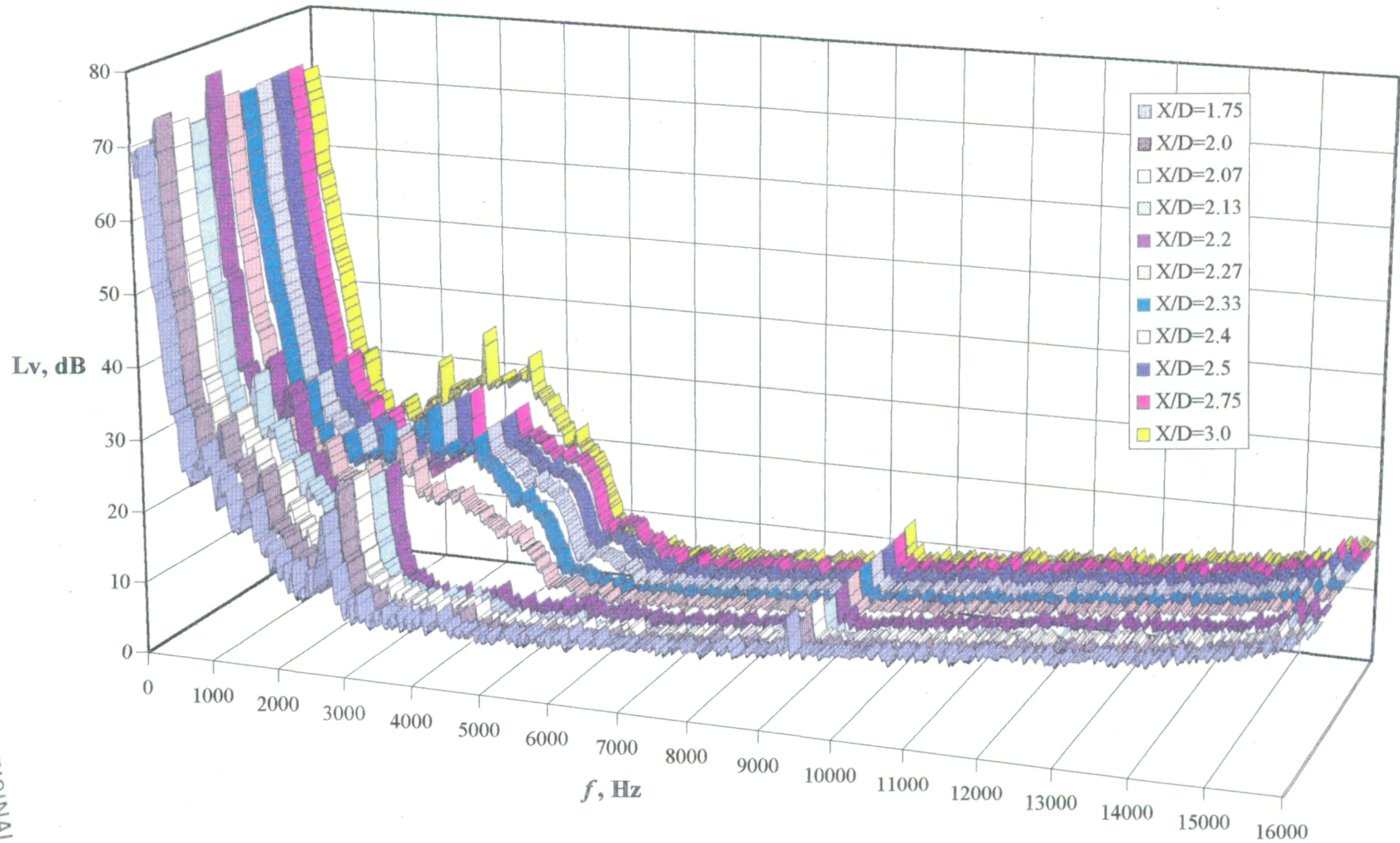


Figure 21. Velocity power spectra over the model with no cavity.  $Re_D = 110,000$

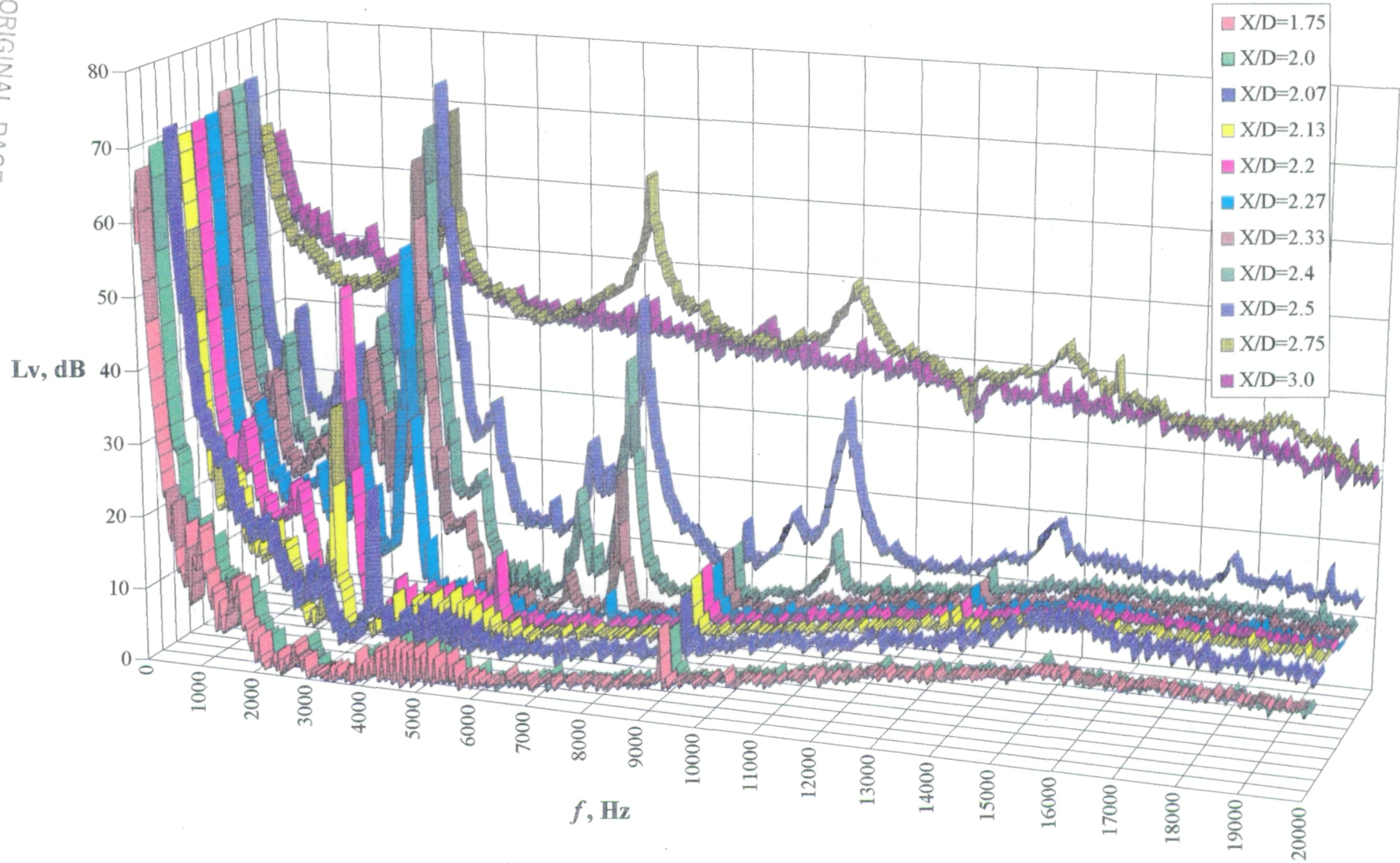


Figure 22. Velocity power spectra over the model with cavity.  $Re_D = 78,000$

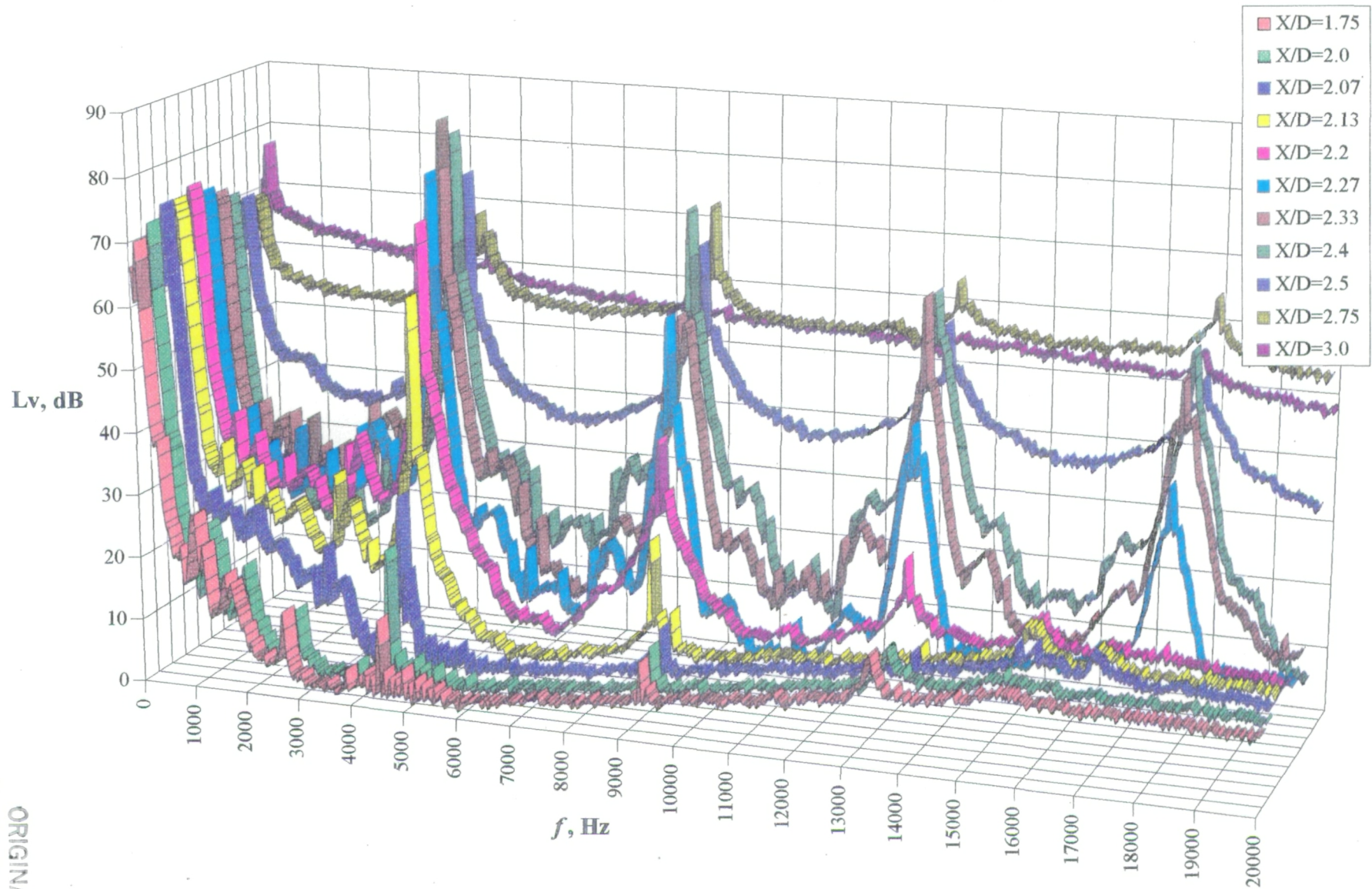


Figure 23. Velocity power spectra over the model with cavity.  $Re_D = 94,000$ .

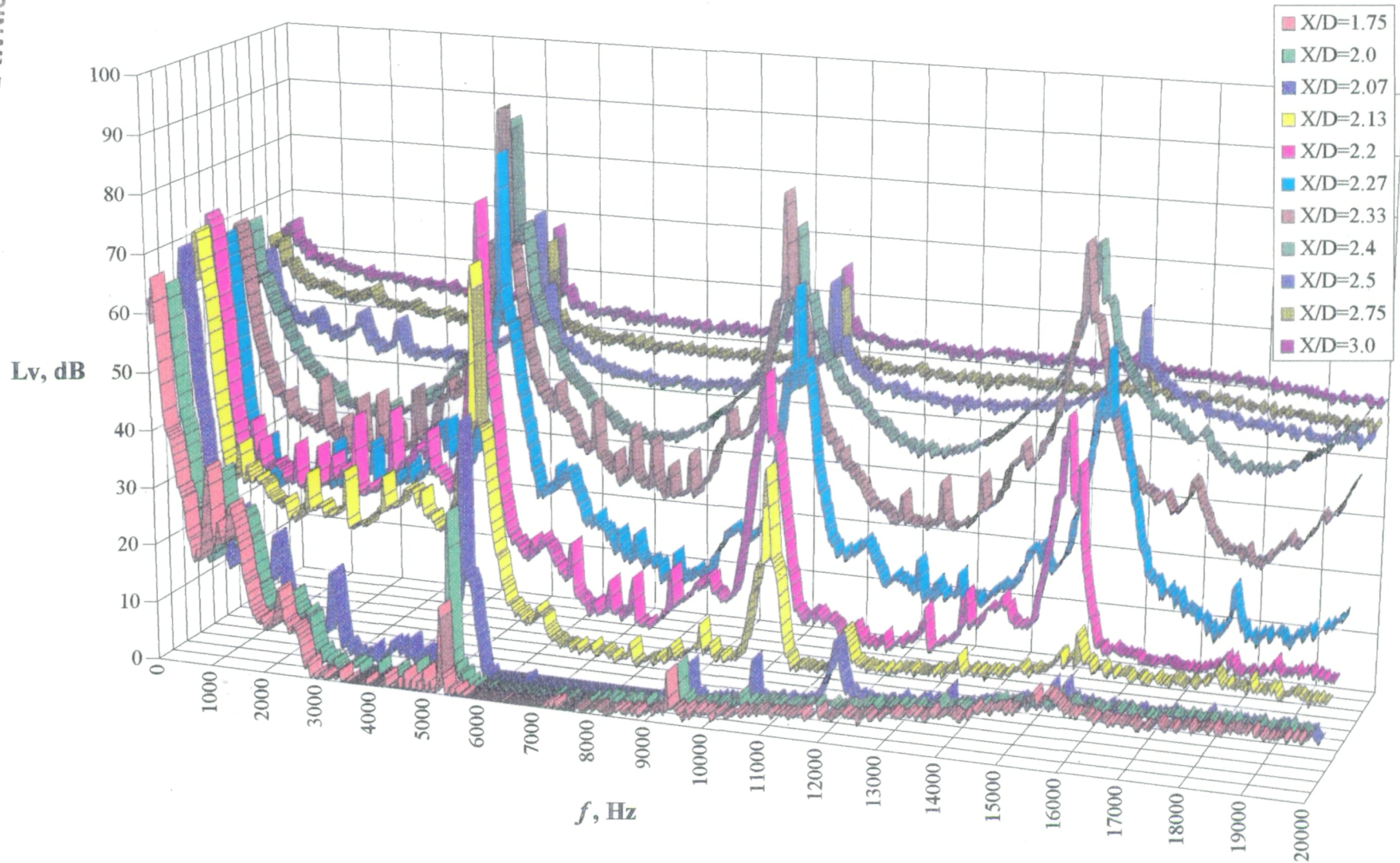


Figure 24. Velocity power spectra over the model with cavity.  $Re_D = 110,000$ .

### **3.3.2 Coherence between velocity and acoustic oscillations**

The measured flow velocity oscillations are strongly coupled with the acoustic signals inside the cavity. This is supported by their coherence shown in figures 25-27. With increasing Reynolds number, these two signals are coherent not only at the dominant frequency but also at its harmonics. While it would be ideal also to have their phase relationships documented to further reveal details of this coupling relationship, this has not been done because the phase calibration between the hot-wire and microphone was very difficult to do.

Note that figures 25-27 also show strong coherence at frequencies other than the fundamentals and their harmonics. They correspond to some weak spectral spikes seen in figures 22-24. Their magnitudes are about two orders-of-magnitude smaller than the dominant oscillations, and their sources have not been identified.

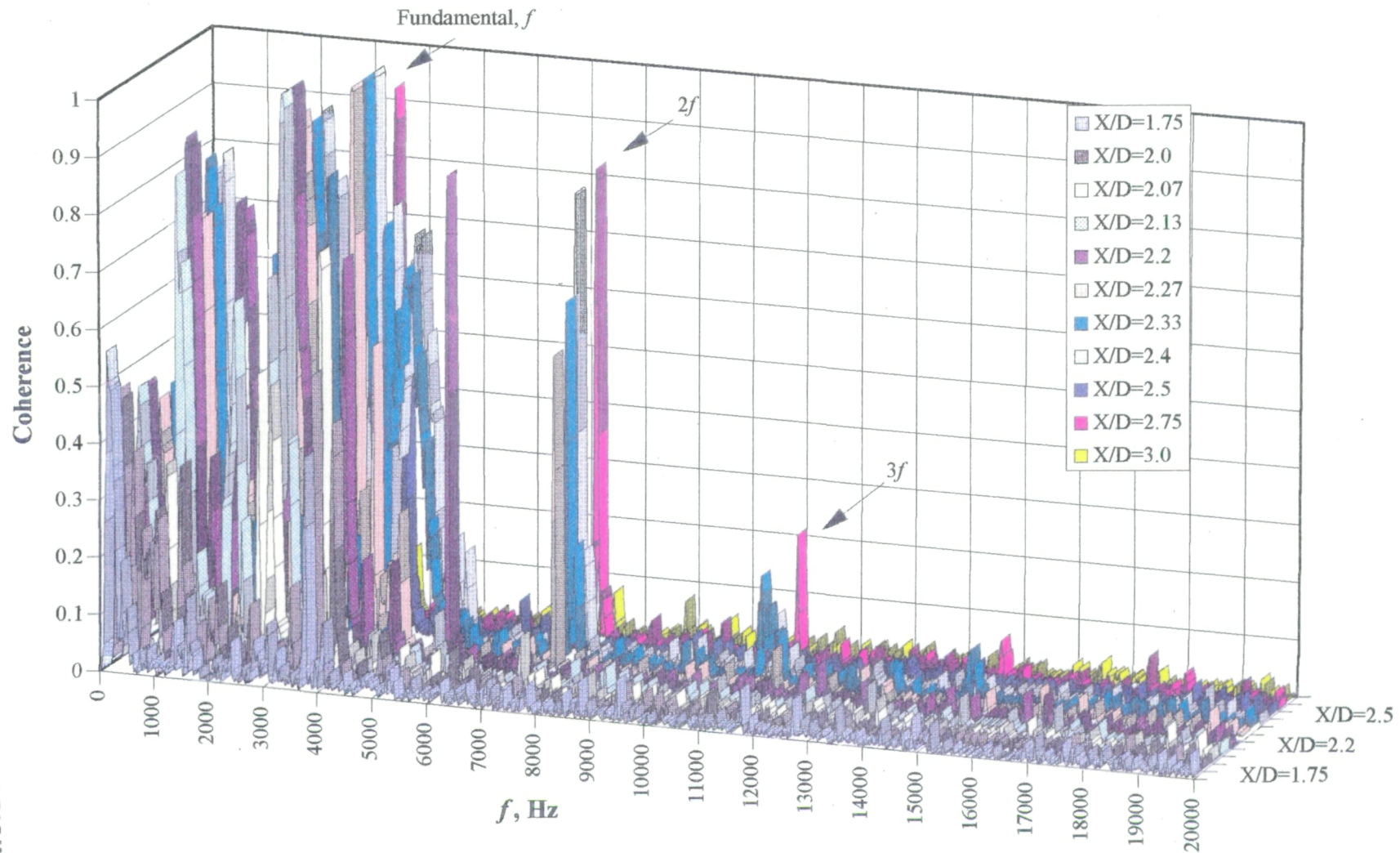


Figure 25. Coherence between acoustic and velocity signals over the model with cavity.  $Re_D = 78,000$ .

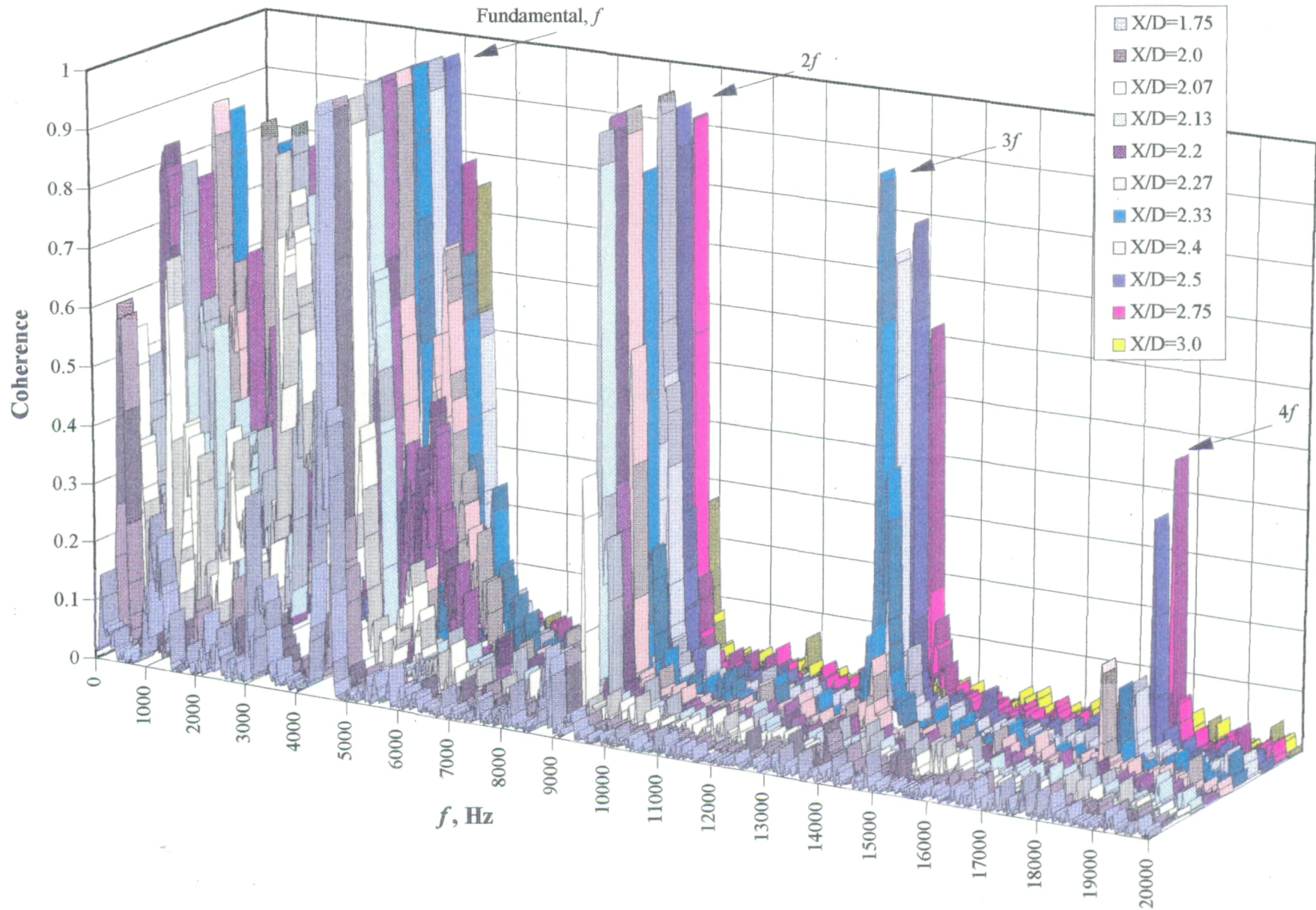


Figure 26. Coherence between acoustic and velocity signals over the model with cavity.  $Re_D = 94,000$ .

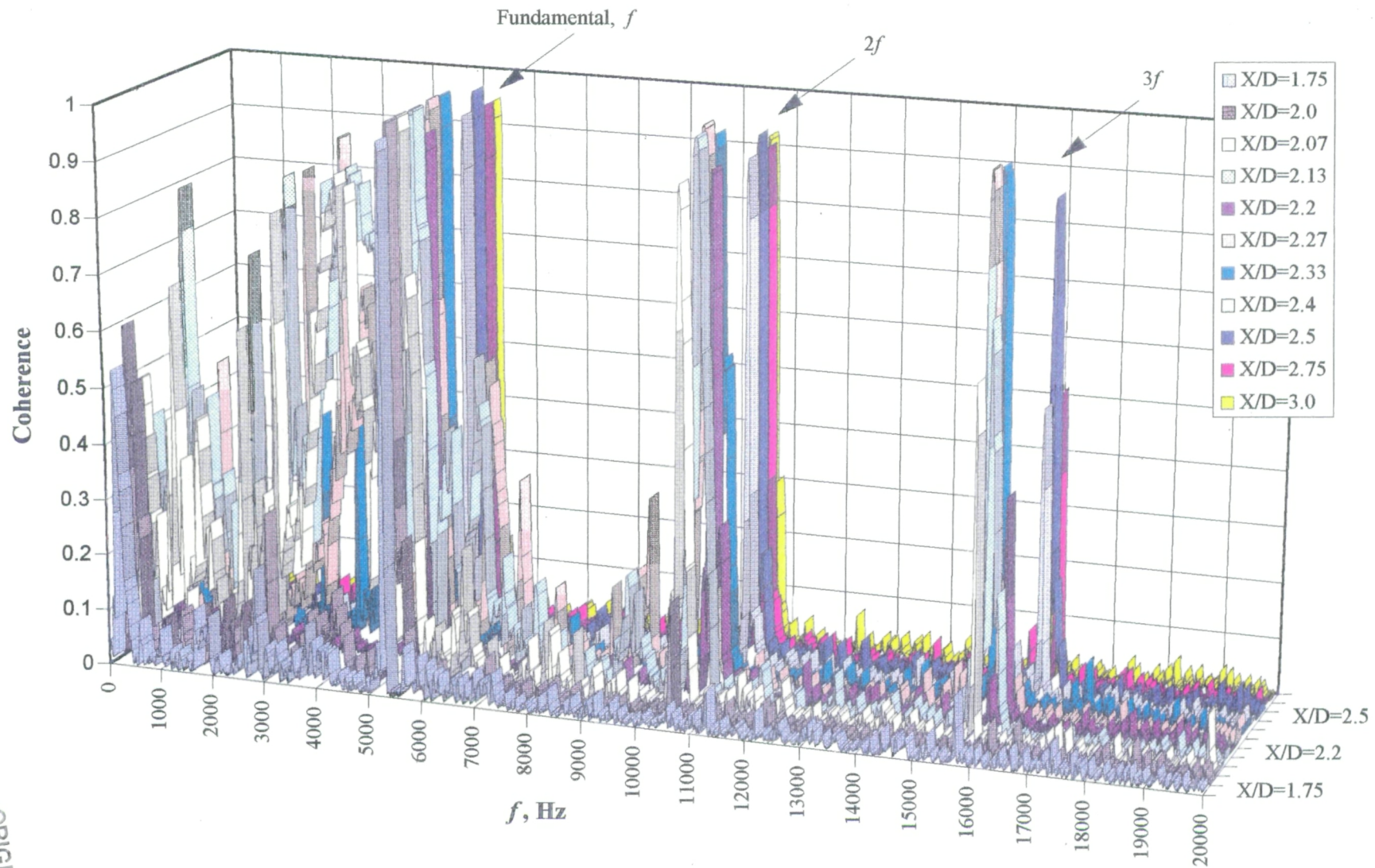


Figure 27. Coherence between acoustic and velocity signals over the model with cavity.  $Re_D = 110,000$ .

ORIGINAL PAGE  
COLOR PHOTOGRAPH

### **3.4 Cavity Acoustic Oscillation Mechanisms**

With all the velocity and acoustic data, one key question that needs to be answered in this investigation was the type of cavity acoustic oscillations observed on the B&K microphones and their generation mechanism(s). As reported in the introduction, Block<sup>5,6</sup> in her rectangular cavity studies has emphasized the interactions between cavity shear layer vortices and the cavity trailing edge and the feedback from there for sustaining cavity shear layer oscillations. She has also suggested the cavity trailing edge as a principal noise source. On the other hand, the screened cavity study by Soderman<sup>10</sup> has shown that the orifice flow oscillations can be coupled with cavity acoustic pressures to generate tones. Since either one of these models appears to be feasible to the B&K microphone cavities, a comparison, starting with cavity oscillation frequencies, was made to examine their feasibility and also to determine the cavity oscillation mechanism(s).

#### **3.4.1 Cavity oscillation frequencies**

As we have seen in previous acoustic spectra (figures 8-10), at any given Mach number, the B&K microphones have shown oscillations at several frequencies. These frequencies are either harmonically or nonharmonically related. For the 1.5 inch microphone model, both its acoustic and velocity spectra have shown one dominant oscillation at a time, along with several harmonics. The dominant oscillation frequencies, when expressed in Strouhal numbers, compares well with Ethembabaoglu's<sup>12</sup> pressure oscillation data measured at the downstream wall of a rectangular cavity. Actually, as shown in figure 28, the two Strouhal numbers of the 1.5 inch model (see figure 11) either match or are close to Ethembabaoglu's dominant Strouhal numbers. Furthermore, as will be seen in section 3.7, when the cavity

screen was removed, both Strouhal numbers of the 1.5 inch model matches Ethembabaoglu's data.

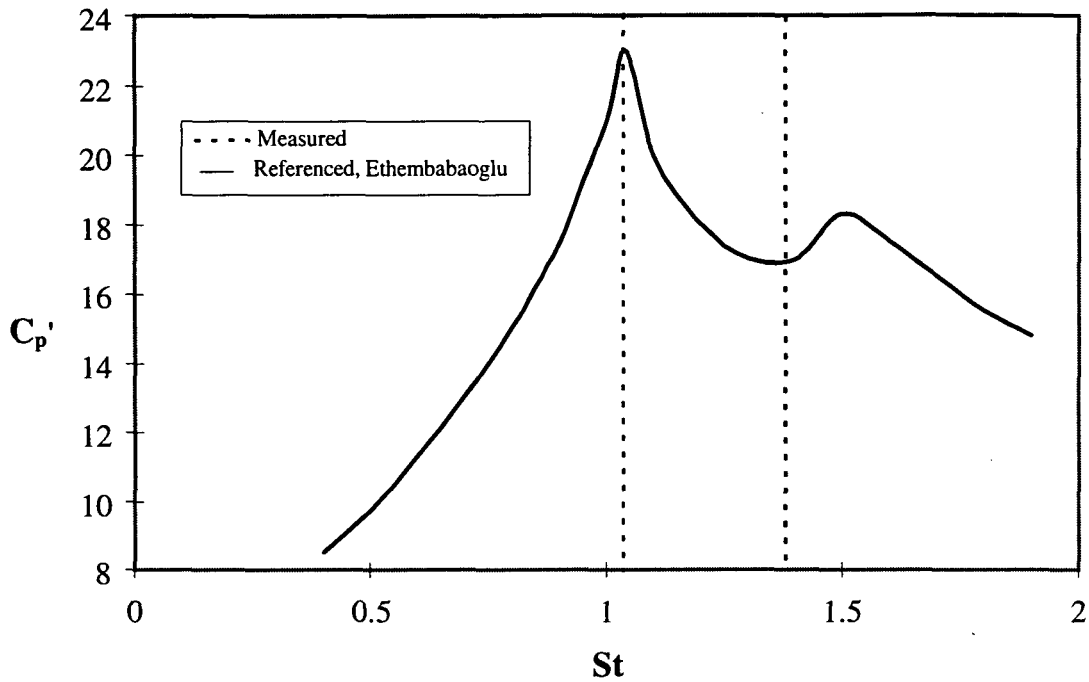


**Figure 28.** Strouhal number comparison of cavity oscillations. The solid line denotes Ethembabaoglu's pressure fluctuation spectrum at the downstream cavity wall of a rectangular cavity. (Reference 12.)

When the Strouhal number is plotted against the cavity length-to-depth ratio in figure 29, as in other cavity flow studies, the Strouhal numbers of the 1.5 inch model again compared well with Ethembabaoglu's rectangular cavity results. In addition, they compare well with Sarohia's shear layer velocity results of an axisymmetric cavity, and Block's far-field acoustic results of a rectangular cavity. Note that all the reference results are for open cavities. Despite their differences in cavity geometry and data type, the Strouhal numbers of the 1.5 inch microphone model appear to match well with the referenced results. This suggests that the B&K microphone cavity, though covered with a mesh screen, appears to behave more like an open cavity.

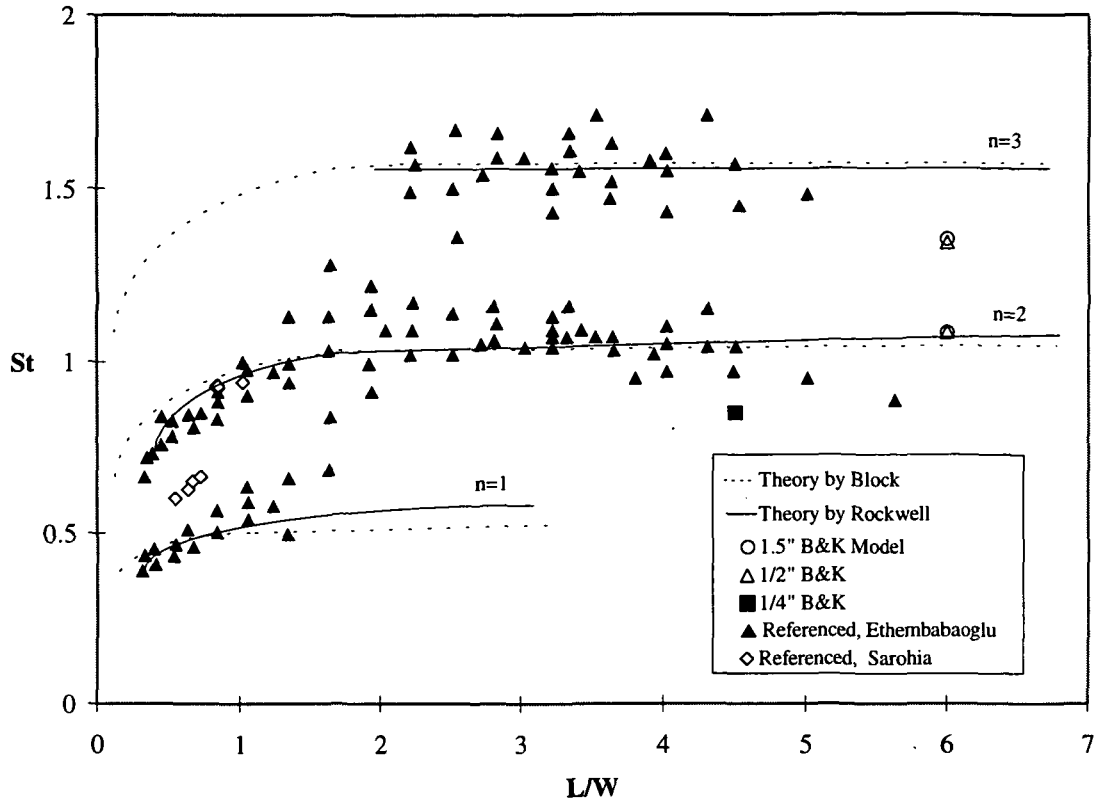


**Figure 29.** Strouhal number vs. cavity aspect ratio. (References 5, 7, 8 and 12.)

This however is not the case for Soderman's screened cavity.<sup>10</sup> In his case, screened and open cavities resonated at completely different frequencies; the differences were as high as 20-30 times. Such differences could readily be explained by his screen porosity in a range from 2.6% to 19.6%, which is far lower than the B&K microphone's mesh porosity at around 50%. Soderman in his study has also suggested that it is the phase coupling between the orifice vortex shedding and cavity acoustic pressures that is responsible for the observed cavity tones. In his model, each orifice is part of the feedback loop to help sustain cavity acoustic resonance, and the cavity trailing edge plays no significant roles in the feedback

loop. Again, the high velocity disturbance intensity measured in the vicinity of the cavity trailing edge of the 1.5 inch model would suggest otherwise.

The fact that the B&K microphone behaves more like an open cavity suggests that cavity shear layer oscillations and their interactions with the cavity trailing edge are essential to the observed cavity oscillations, acoustic or hydrodynamic. It also allows us to gain more insight of the B&K microphone cavity oscillations by examining some cavity flow visualization studies.

### **3.4.2 Trailing-edge vortex shedding**

It is well known that a carefully planned flow visualization could provide insight of a complex flow phenomenon, like cavity oscillations. This has not been possible for the B&K model because of the screen over its cavity. A smoke visualization done by Sarohia<sup>7</sup> of flow oscillations over an axisymmetric, shallow cavity without a screen has therefore been used to provide the much needed insight of the microphone cavity flow.

As he has observed, the mean streakline of the cavity shear layer shows little oscillations until it is very close to the cavity trailing edge, where strong oscillations occur. The mean streakline oscillates in and out of the cavity at the cavity oscillation frequency in the vicinity of cavity trailing edge. As the streakline deflects into the cavity, the shear layer rolls up into a vortex. This vortex is later shed from the cavity when the streakline deflects outward.

Sarohia's description of cavity oscillatory flow appears to fit the present results. His observation of vortices is consistent with the inflection point seen in the mean velocity profile near the cavity trailing edge. The strong interactions between the vortices and cavity trailing edge are also consistent with the high velocity disturbance intensity observed in that region. Following this flow description, it seems natural to conclude that the measured acoustic tones are the consequence of periodic vortices impinging on the cavity trailing edge. The impinging in turn provides the necessary acoustic feedback pressure to enhance the shear layer disturbances at the separation point. This is the fundamental mechanism for self-sustaining cavity shear layer oscillations. Although no flow visualization was done in this experiment to compare with Sarohia's flow observations, the evidences so far, especially the Strouhal number plots in figures 28 and 29, are consistent with this flow description. Consequently the interactions between cavity shear layer oscillations and the cavity trailing edge are the likely cause of the self-sustained acoustic oscillations. This, in fact, is the essence of Block's vortical-acoustical feedback model.

### **3.4.3 Coupling with cavity acoustic resonance**

Despite the importance of cavity shear layer oscillations and their interactions with the cavity trailing edge, one important question to the present study was whether the cavity shear layer oscillations are coupled with acoustic resonant modes inside the cavity. Experimentally, cavity acoustic resonant modes could be determined directly by measuring standing waves inside the cavity. This however was not feasible because the microphone size was close to the acoustic wavelengths of interest. Consequently, a comparison was made with the

frequencies of possible acoustic resonant modes of a closed cylindrical enclosure of length  $L$  and radius  $R$  computed with the following equation<sup>16</sup>:

$$f = \frac{c}{2\pi} \left( \frac{\lambda_{jk}^2}{R^2} + \frac{i^2 \pi^2}{L^2} \right)$$

Table 1 shows part of the computed frequencies for comparison with the present data. As seen in the table, the lowest frequency for the length mode is 15.3 kHz ( $i = 1, j = 0, k = 0$ ), which is much higher than the dominant oscillation frequencies at 3,750 Hz, 4,500 Hz, and 5,325 Hz for  $Re_D = 78,000, 94,000, \text{ and } 110,000$ , respectively (see figure 10). The 5,325 Hz, on the other hand, are close to the lowest frequency of 5,234 Hz ( $i = 0, j = 1, k = 0$ ) for the radial mode. This suggests that for certain modes the cavity shear layer oscillation frequencies could be close to acoustic resonant frequencies inside the cavity. Note that the equation used is for a cylindrical enclosure. But a similar equation for rectangular cavity has given reasonable estimates of cavity resonant frequencies in previous experiments.<sup>8,10</sup> Consequently, as we believe, when frequencies match, the cavity shear layer oscillations could couple with cavity acoustic resonance to generate tones.

Radial Modes							
$\lambda_{jk}$	$j$						
$k$	0	1	2	3	4	5	6
0	0	5234	8682	11943	15116	18238	21324
1	10892	15155	19063	22785	26387	29905	33359
2	19943	24266	28340	32253	36051	39761	43403
3	28919	33276	37439	41463	45381	49215	52980
Longitudinal Modes							
$i$	1	2	3	4	5	6	
$f$	15,327	30,654	45,981	61,308	76,635	91,962	

**Table 1.** Lowest possible radial and longitudinal acoustic resonant frequencies, in Hertz, calculated for a cylindrical enclosure resembling the B&K cavity.

### **3.4.4 Hydrodynamic pressure oscillations**

It is known that the microphone inside the cavity can record hydrodynamic pressure oscillations. Since large velocity disturbance intensities were measured near the cavity trailing edge, one should expect strong velocity and pressure oscillations inside the cavity. Were this the case, the microphone signals should show spectral peaks at cavity shear layer oscillation frequencies, as have been seen in this experiment. This is also consistent with the high coherence observed between the hot-wire and microphone signals, and it applies to all the oscillation frequencies that have been recorded.

The above argument suggests that besides impingement noise at the cavity trailing edge, the microphone signals recorded in the B&K microphone cavity should include the hydrodynamic pressure oscillations. They could also include cavity acoustic pressure oscillations when the shear layer oscillation frequencies match acoustic resonant modes.

### **3.5 Effect of Adverse Pressure Gradient**

At the early stage of this experiment, it was suspected that perhaps the adverse pressure gradient near the cavity leading edge is the main difference between the FITE and B&K microphones. The FITE's forebody is leveled near the cavity leading edge; it has essentially zero pressure gradient, as compared to the B&K microphones' adverse pressure gradients. This, however, may not be the case. Sarohia, in his experiment, tested three ogive forebodies of length-to-diameter ratios at 0.6, 1.12, and 2.12, respectively. As he found out, as long as  $L/\delta_0$  ( $L$ , cavity length;  $\delta_0$ , boundary layer thickness at the separation point) is kept constant and above a minimum value of about 5.25 by changing flow speed, the cavity oscillations

occur and their Strouhal numbers stay the same. Since different ogive forebody shapes have different adverse pressure gradients, his results would suggest that the adverse pressure gradient does not have a direct effect on the cavity oscillations. Instead, what is important is the boundary layer thickness at the separation point. Since the FITE's forebody is three times longer than the B&K microphone forebody, perhaps its success in eliminating cavity tones is due to boundary layer turbulence. The turbulence could increase boundary layer thickness at the separation point such that  $L/\delta_0$  is decreased below the minimum value.

### **3.6 Effect of Turbulence**

The potential effect of boundary layer turbulence was qualitatively investigated by tripping the flow on the apex of the B&K model. An annular 0.125 inch wide stripe was first masked at  $X/D=1.75$ , and an adhesive was applied to the stripe surface. Then, using a salt shaker, the stripe was sprinkled with 0.010-0.015 inch glass beads. The formed rough annulus tripped the boundary layer, and the resulting flow had a profound effect on the cavity acoustic oscillations - it eliminates them entirely. Both the acoustic and velocity power spectra showed no signs of oscillations. Meanwhile, their noise floors increased dramatically. This result has suggested that the FITE's success in eliminating tones could be due to its boundary layer turbulence. Turbulence might have thickened the boundary layer at the separation point so that the  $L/\delta_0$  ratio is below 5.25. Or it might have weakened the shear layer vortices or lifted them to miss impinging on the cavity trailing edge.

### 3.7 Effect of Screen

Throughout the discussion, comparisons have often been made with cavity flows without screens. Resemblance among cavity oscillation Strouhal numbers perhaps has already implanted a foregone conclusion that cavity screen only plays a minor role in determining the oscillation frequencies. Having said this, it is nonetheless interesting to know how much the screen would affect the cavity acoustic oscillations. In an attempt to examine this, the screen was removed completely from the cavity. As found in the experiment, initially, at  $Re_D = 110,000$ , no tones were recorded. The tones however became quite loud at a lower Reynolds number of about 45,000. As shown in figure 30, the acoustic spectra shows a distinct tone at 1.8 kHz ( $A_1$ ) along with several harmonics ( $A_2$ - $A_7$ ).

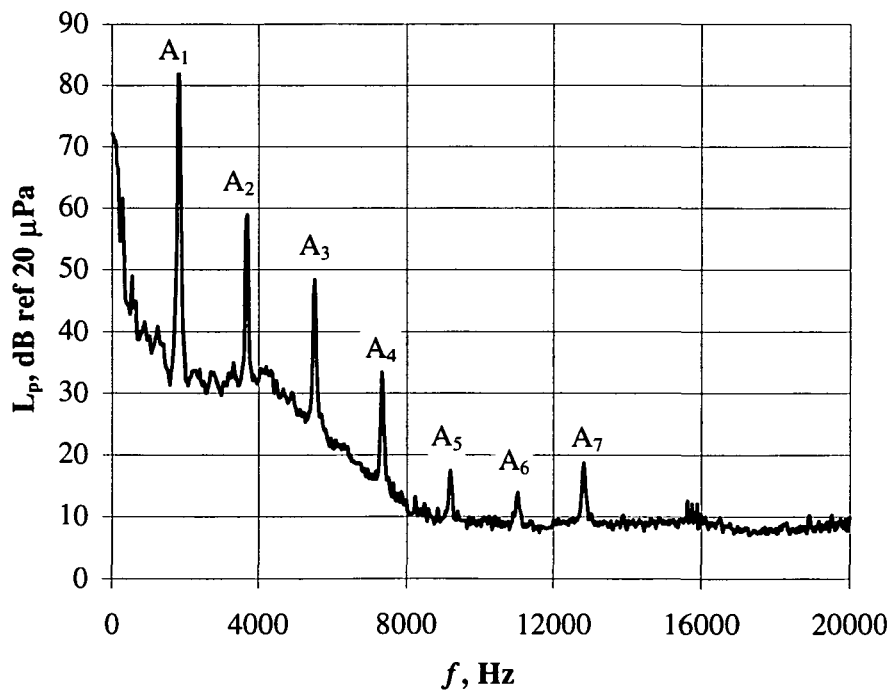


**Figure 30.** Acoustic power spectra of the model with screen removed:  $A_1$  = dominant tone at  $Re_D = 45,000$ ;  $A_2$  -  $A_7$  = harmonics of  $A_1$ .

As before, the intensity of velocity oscillations increases in strength with the increased distance from the cavity leading edge until it reaches a maximum in the vicinity of the cavity trailing edge, as shown in figure 31. Again, the acoustic and velocity signals are coherent at the dominant oscillation frequency and its harmonics (see figure 32).

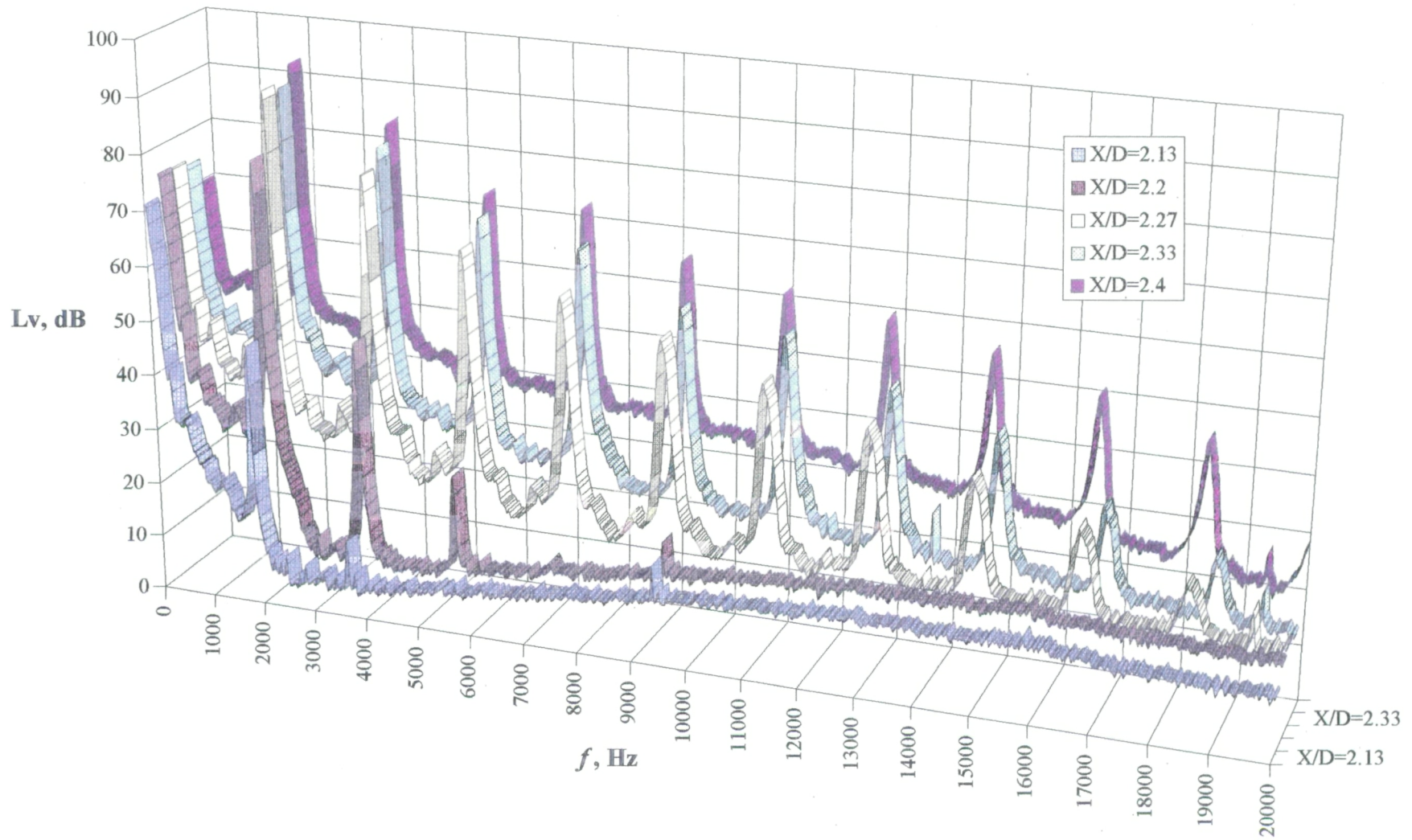
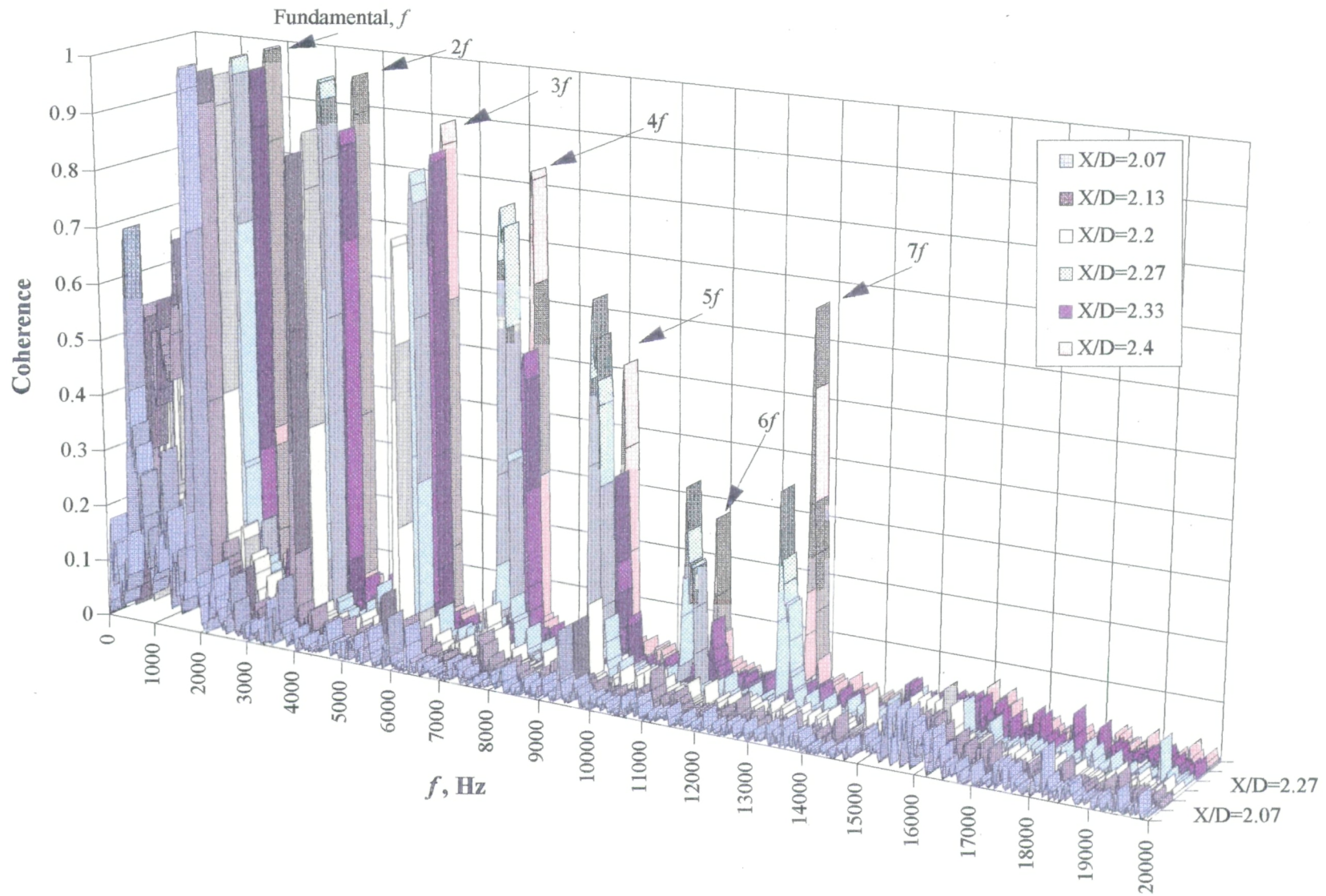
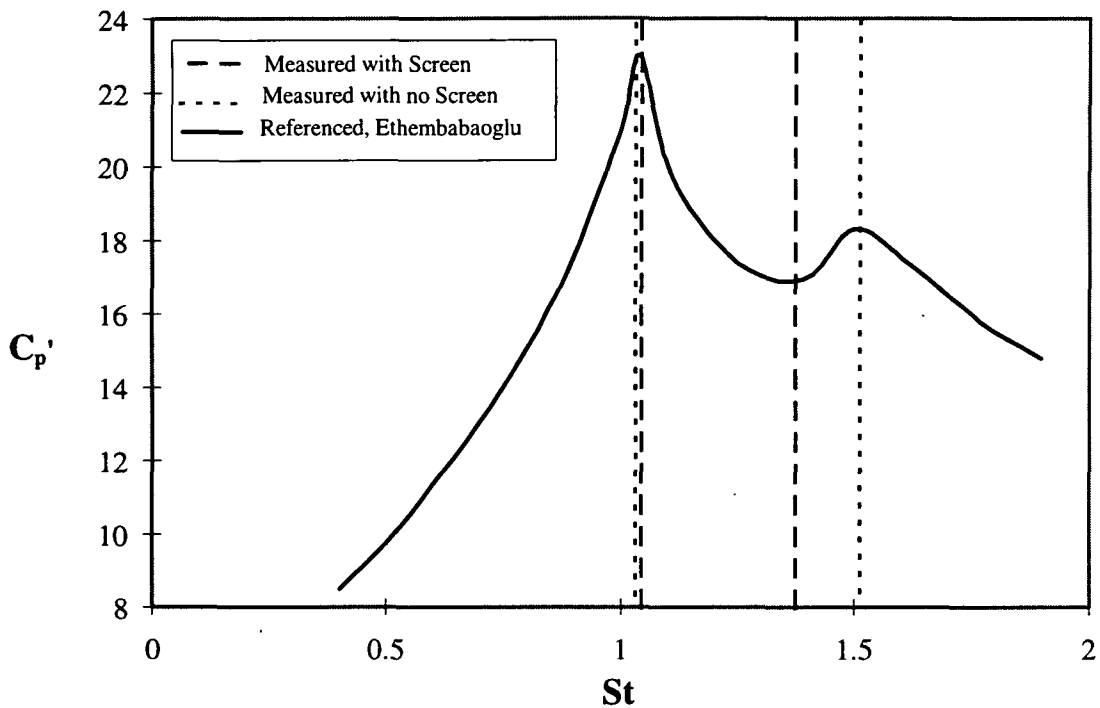


Figure 31. Velocity power spectra over the model with no screen.  $Re_D = 45,000$



**Figure 32.** Coherence between acoustic and velocity signals over the model with no screen.  $Re_D = 45,000$ .

Despite lower Reynolds numbers, the Strouhal numbers match the values found by Ethembabaoglu as shown in figure 33. The screen might have changed the local shear layer properties, made it thinner as suggested in some earlier studies on slotted cavities,<sup>8</sup> and changed the oscillation frequencies. The fundamental cavity oscillation mechanism however appears to remain the same.



**Figure 33.** Strouhal number comparison of cavity oscillations of the 1.5 inch model with and without the screen. The solid line denotes Ethembabaoglu's pressure fluctuation spectrum at the downstream cavity wall of a rectangular cavity. (Reference 12.)

#### 4. CONCLUSIONS

An experiment has been conducted to investigate the flow-induced acoustic oscillations of the B&K in-flow microphones. The results strongly suggest the B&K microphone cavity behaves more like an open cavity. Their cavity acoustic oscillations are likely caused by strong interactions between cavity shear layer and the cavity trailing edge. But the results also suggest that cavity shear layer oscillations could be coupled with cavity acoustic resonance to generate tones.

Detailed flow velocity measurements over the cavity screen have shown inflection points in the mean velocity profiles and high disturbance and spectral intensities in the vicinity of the cavity trailing edge. These results on one hand are the evidence for strong interactions between cavity shear layer oscillations and the cavity trailing edge. They also suggest that beside acoustic signals, the microphone inside the cavity has likely recorded hydrodynamic pressure oscillations, too.

The results also suggest that the forebody shape does not have a direct effect on cavity oscillations. For the FITE microphone, it is probably the forebody length and the resulting boundary layer turbulence that have made it work. Turbulence might have thickened the boundary layer at the separation point, weakened the shear layer vortices, or lifted them to miss impinging on the cavity trailing edge. In addition, the study shows that the cavity screen can modulate the oscillation frequency but not the cavity acoustic oscillation mechanisms.

Though without a flow visualization due to the cavity screen, a cavity oscillation model based on Sarohia's smoke visualization study of an open cavity seems to fit the present data. In this flow model, the cavity shear layer oscillates strongly when approaching the cavity trailing edge, where the shear layer in one cycle deflects into the cavity, rolls up into a vortex, and later sheds the vortex out of the cavity. While this flow description to some extent is feasible for the microphone cavity, it is also more than what could be supported by this study. A flow visualization study conducted simultaneously with an acoustic measurement would certainly be useful to the missing details.

## REFERENCES

---

1. Jaeger, S. M., Allen, C. S. and Soderman, P. T., "Reduction of Background Noise in the NASA Ames 40- By 80-Foot Wind Tunnel," CEAS/AIAA-95-152, June 1995.
2. Hickey, D. H. and Williams, J., "Noise Measurements in Wind Tunnels Workshop Summary," NASA Technical Memorandum 84219, September 1982.
3. Allen, C. S. and Soderman, P. T., "Aeroacoustic Probe Design for Microphone to Reduce Flow-Induced Self-Noise," AIAA paper 93-4343, October 1993.
4. Glover, B.M. and Shivashankara, B.N., "Aeroacoustic Testing in Wind Tunnels," AIAA paper 86-1886, AIAA 10th Aeroacoustic Conference, July 1986.
5. Block, P. J. W., "Measurements of the Tonal Component of Cavity Noise and Comparison with Theory," NASA Technical Paper 1013, 1977.
6. Block, P. J. W., "Noise Response of Cavities of Varying Dimensions at Subsonic Speeds," NASA TN D-8351, 1976.
7. Sarohia, V., "Experimental Investigation of Oscillations in Flows Over Shallow Cavities," AIAA Journal, Vol. 15, No. 7, April 1977.
8. Rockwell, D. and Naudascher, E., "Review - Self-Sustaining Oscillations of Flow Past Cavities," Journal of Fluid Mechanics, Vol. 100, June 1978, pp. 152-165.
9. Soderman, P. T., "Design and Performance of Resonant-Cavity Parallel Baffles for Duct Silencing," Noise Control Engineering, Vol. 17, No. 1, July-Aug. 1981, pp. 12-21.
10. Soderman, P. T., "Flow Induced Resonance of Screen-Covered Cavities," NASA Technical Paper 3052, October 1990.
11. McMasters, J. H., Nordvick, R. H., Henderson, M. L., and Sandvig, J. H., "Two Airfoil Sections for Low Reynolds Number," Vol. VI, No.4, XVIIth OSTIV Congress, Paderborn, Germany, May 1981.
12. Ethembabaoglu, S., "On Fluctuating Flow Characteristics in the Vicinity of Gate Slots," Division of Hydraulic Engineering, University of Trondheim, Norwegian Institute of Technology, June 1973.
13. Meyer, Mechel and Kurtze, "Experiments on the Flow and Sound Attenuation in Absorbing Ducts," Journal of Acoustical Society of America, Vol. 30, 1958, pp. 165.
14. Schlichting, H., "Boundary-Layer Theory," Seventh Edition, McGraw-Hill, Inc., 1987.

15. Arakeri, V. H., "A Note on the Transition Observations on an Axisymmetric Body and Some Related Fluctuating Wall Pressure Measurements," *Journal of Fluids Engineering*, March 1987, pp. 82-86.

16. Beranek, L. L., and Vér, I. L., "Noise and Vibration Control Engineering," John Wiley & Sons, Inc., 1992.